National Library of Canada
Bibliothèque nationale du Canada

Acquisitions and Bibliographic Services Branch
Direction des acquisitions et des services bibliographiques

395 Wellington Street
Ottawa, Ontario
K1A 0N4

395, rue Wellington
Ottawa (Ontario)
K1A 0N4

Your file Votre référence

Our file Notre référence

## NOTICE

The quality of this microform is heavily dependent upon the quality of the original thesis submitted for microfilming. Every effort has been made to ensure the highest quality of reproduction possible.

If pages are missing, contact the university which granted the degree.

Some pages may have indistinct print especially if the original pages were typed with a poor typewriter ribbon or if the university sent us an inferior photocopy.

Reproduction in full or in part of this microform is governed by the Canadian Copyright Act, R.S.C. 1970, c. C-30, and subsequent amendments.

## AVIS

La qualité de cette microforme dépend grandement de la qualité de la thèse soumise au microfilmage. Nous avons tout fait pour assurer une qualité supérieure de reproduction.

S'il manque des pages, veuillez communiquer avec l'université qui a conféré le grade.

La qualité d'impression de certaines pages peut laisser à désirer, surtout si les pages originales ont été dactylographiées à l'aide d'un ruban usé ou si l'université nous a fait parvenir une photocopie de qualité inférieure.

La reproduction, même partielle, de cette microforme est soumise à la Loi canadienne sur le droit d'auteur, SRC 1970, c. C-30, et ses amendements subséquents.

Canada

UNIVERSITY OF ALBERTA

# BICEPSTRAL DECONVOLUTION OF THE SURFACE ELECTROMYOGRAM

BY

MARK D. DOES

©

A THESIS SUBMITTED TO

THE FACULTY OF THE GRADUATE STUDIES AND RESEARCH

IN PARTIAL FULFILLMENT OF THE REQUIREMENTS FOR THE DEGREE OF

MASTER OF SCIENCE

DEPARTMENT OF ELECTRICAL ENGINEERING

EDMONTON, ALBERTA

SPRING 1993

National Library of Canada
Bibliothèque nationale du Canada

Acquisitions and Bibliographic Services Branch
Direction des acquisitions et des services bibliographiques

395 Wellington Street
Ottawa, Ontario
K1A 0N4

395, rue Wellington
Ottawa (Ontario)
K1A 0N4

Your file Votre référence

Our file Notre référence

The author has granted an irrevocable non-exclusive licence allowing the National Library of Canada to reproduce, loan, distribute or sell copies of his/her thesis by any means and in any form or format, making this thesis available to interested persons.

L'auteur a accordé une licence irrévocable et non exclusive permettant à la Bibliothèque nationale du Canada de reproduire, prêter, distribuer ou vendre des copies de sa thèse de quelque manière et sous quelque forme que ce soit pour mettre des exemplaires de cette thèse à la disposition des personnes intéressées.

The author retains ownership of the copyright in his/her thesis. Neither the thesis nor substantial extracts from it may be printed or otherwise reproduced without his/her permission.

L'auteur conserve la propriété du droit d'auteur qui protège sa thèse. Ni la thèse ni des extraits substantiels de celle-ci ne doivent être imprimés ou autrement reproduits sans son autorisation.

ISBN 0-315-82136-1

Canada

UNIVERSITY OF ALBERTA

RELEASE FORM

NAME OF AUTHOR: Mark D. Does

TITLE OF THESIS: Bicepstral Deconvolution of the Surface Electromygram

DEGREE: Master of Science

YEAR THIS DEGREE GRANTED: 1993

Permission is hereby granted to the University of Alberta Library to reproduce single copies of this thesis and to lend or sell such copies for private, scholary or scientific research purposes only.

The author reserves all other publication and other rights in association with the copyright in the thesis, and except as herinbefore provided neither the thesis nor any substantial portion thereof may be printed or otherswise reproduced in any material form whatever without the author's prior written permission

Mark D. Does
#1101 8315 105 st.
Edmonton AB
T6E 4H4

Date: 04/20/93

UNIVERSITY OF ALBERTA

FACULTY OF GRADUATE STUDIES AND RESEARCH

The undersigned certify that they have read, and recommend to the Faculty of Graduate Studies and Research for acceptance, a thesis entitled **Bicepstral Deconvolution of the Surface Electromyogram** submitted by **Mark D. Does** in partial fulfillment of the requirements for the degree of **Master of Science**.

Dr. Z. J. Koles (Supervisor)

Dr. R. E. Rink

Dr. R. E. Snyder

Date: 9/20/93

*This thesis is dedicated to my parents,*
*Sharon and Doug Does: my mentors and friends.*

## ABSTRACT

A new method of analyzing the surface electromyogram (SEMG) has been developed, in which each SEMG is characterized by a single "representative surface motor unit action potential" (RSMUAP). This method is based upon modelling the SEMG as the output of a linear time-invariant system that has an impulse response equal to the RSMUAP. The RSMUAP can then be recovered from the SEMG using a technique called bicepstral deconvolution. Bicepstral deconvolution is a homomorphic method of separating signals that is based upon the bispectrum. Using the bispectrum, rather than the power spectrum is required for a non-minimum phase estimation of the RSMUAP. The bispectrum has the added benefit of being zero for Gaussian signals, making it well suited for analyzing noisy data. Simulations indicate that this new method of SEMG analysis should be effective for detecting the progression of myopathy.

## ACKNOWLEDGEMENTS

Thank you, Dr. Zoltan Koles, for being a thoughtful and consientious supervisor.

I'd like to thank Professor Y.J. Kingma for giving me the opportunity to enter graduate school and Dr. Z.J. Koles for graciously taking the reigns upon Prof. Kingma's departure. I'd like to thank Dr. R. Lawson for his efforts to minimize the complications of my student life. And I'd like to thank Dr. R. Rink and Dr. R. Snyder for being members of my examining committee.

I'd like to express my sincere pleasure and graditude to the many friendly people who have helped me through my degree. This long list includes: Dave Rudyk, Martin Mintchev, Clarence Dziadyk, Ion Buicliu, Elsie Mahe, the EE office staff: Shirley, Michelle, Carla, and Caroline, Mark Astridge, Nora O'Neill, Dr. V. Gourishankar, and Dr P. Allen.

Last but not least, I'd like thank my parents, my sister, Karon, my very good friend Brett Barnet, and my fiancé, Leanne Clare, for their endless support.

TABLE OF CONTENTS

Page

ABSTRACT
LIST OF TABLES
LIST OF ILLUSTRATIONS
LIST OF ABBREVIATIONS

Chapter 1 Introduction ..... 1
The Motor Unit Action Potential ..... 1
Electromyography ..... 3
The Surface EMG ..... 5
Chapter 2 Non-Minimum Phase Deconvolution ..... 9
Introduction ..... 9
Moments and Cumulants ..... 10
The Bispectrum ..... 15
The Homomorphic method ..... 20
The Bicepstral method ..... 25
Chapter 3 Modelling ..... 31
Introduction ..... 31
The Synthesis Model ..... 31
Modelling Healthy SMUAPs ..... 32
Modelling Diseased SMUAPs ..... 36
Results of SMUAP simulations ..... 37
SEMG Modelling ..... 39
The Analysis Model ..... 47
Signal Requirements ..... 51
Chapter 4 Methods and Results ..... 55
Parameter Determination ..... 55
The Algorithm ..... 58

Experiments ..... 59
Results ..... 61
Chapter 5 Discussion ..... 76
Introduction ..... 76
RSMUAPs' Reflection of Myopathy ..... 76
RSMUAPs versus MUAPs ..... 77
Bicepstral Deconvolution for Estimating RSMUAPs ..... 78
Modelling Variations ..... 80
Conclusion ..... 83
REFERENCES ..... 85

## LIST OF TABLES


| Table | | Page |
|---|---|---|
| Table 3.1 | Tripole characteristics | 33 |
| Table 3.2 | The distribution of MU centers | 43 |
| Table 4.1 | Classification matrix for noise-free RSMUAPs | 65 |
| Table 4.2 | Classification accuracy for noise-free RSMUAPs | 65 |
| Table 4.3 | Classification matrix for noisy RSMUAPs | 69 |
| Table 4.4 | Classification accuracy for noisy RSMUAPs | 69 |

## LIST OF ILLUSTRATIONS


| Figure | | Page |
|---|---|---|
| Figure 2.1 | The system block diagram. | 9 |
| Figure 2.2 | A homomorphic system for deconvolution | 21 |
| Figure 2.3 | Example signals for homomorphic deconvolution | 22 |
| Figure 2.4 | The complex cepstra of example signals. | 23 |
| Figure 2.5 | Decomposition of a mixed phase impulse reponse into its minimum phase and maximum phase components | 25 |
| Figure 3.1 | The double tripole model of the surface-measured SFAP | 32 |
| Figure 3.2 | Tripole unit | 33 |
| Figure 3.3 | Simulated SMUAPs | 38 |
| Figure 3.4 | Simulated SEMG block diagram | 39 |
| Figure 3.5 | A cross section of muscle. | 42 |
| Figure 3.6 | Stage 1 simulated SMUAPs -- 20 per graph. | 44 |
| Figure 3.7 | Stage 5 simulated SMUAPs -- 20 per graph. | 45 |
| Figure 3.8 | Stage 9 simulated SMUAPs -- 20 per graph. | 46 |
| Figure 3.9 | A pictorial description of the synthesis model | 47 |
| Figure 3.10 | A comparison of normalized SMUAPs | 49 |
| Figure 3.11 | Simulated RSMUAPs | 50 |
| Figure 3.12 | The characteristics of the simulated firing signal compared with a Gaussian sequence. | 53 |
| Figure 3.13 | The magnitude bispectra of skewed and non-skewed signals | 54 |
| Figure 4.1 | Power spectra of simulated SEMG | 56 |
| Figure 4.2 | Stage 1 third order cumulants of a simulated SEMG | 57 |
| Figure 4.3 | Stages 5 and 9 third order cumulants of simulated SEMGs | 58 |
| Figure 4.4 | Stage 1 RSMUAPs | 62 |
| Figure 4.5 | Stage 5 RSMUAPs | 63 |
| Figure 4.6 | Stage 9 RSMUAPs | 64 |
| Figure 4.7 | Stage 1 Noisy RSMUAPs | 66 |
| Figure 4.8 | Stage 5 Noisy RSMUAPs | 67 |

Figure 4.9 Stage 9 Noisy RSMUAPs ..... 68
Figure 4.10 Noisy RSMUAPs from SEMGs with varying SNRs. ..... 70
Figure 4.11 Stage 1 Model B RSMUAPs ..... 71
Figure 4.12 Stage 5 Model B RSMUAPs ..... 72
Figure 4.13 Stage 9 Model B RSMUAPs ..... 73
Figure 4.14 The magnitude bispectra of stationary and non-stationary firing signals ..... 74
Figure 4.15 Estimated RSMUAPs from SEMGs with stationary and non-stationary firing signals ..... 75

## LIST OF ABBREVIATIONS

| | |
|---|---|
| MU | Motor Unit |
| SFAP | Single Fibre Action Potential |
| MUAP | Motor Unit Action Potential |
| EMG | Electromyogram |
| MUAPT | Motor Unit Action Potential Train |
| ADEMG | Automatic Decomposition Electromyogram |
| MVC | Maxmimum Voluntary Contraction |
| SEMG | Surface Electromyogram |
| SMUAP | Surface-measured Motor Unit Action Potential |
| AR | Autoregressive |
| LTI | Linear and Time-Invariant |
| FFT | Fast Fourier Transform |
| RSMUAP | Representative Surface-measured Motor Unit Action Potential |

# Chapter 1
# Introduction

*The Motor Unit Action Potential* [1]

Nerve cells transmit information via the propagation of action potentials along the axon of the cell. A "sodium pump" inside nerve and muscle cell membranes pumps sodium ions out of the cell, leaving the inside of the cell at a resting potential of about -70mV, relative to intercellular space. When the cell is stimulated, raising the membrane potential above a threshold of roughly -60mV, an irreversible process known as an action potential begins. Sodium channels in the cell membrane open and allow an influx of $Na^+$ ions which raises the membrane potential rapidly to about +25mV -- a process known as depolarization. This rise in potential is then thwarted by opening potassium channels which allow an efflux of $K^+$ ions, and repolarization begins. Closing of the sodium channels then speeds repolarization, which is followed by a small hyperpolarization (i.e., membrane potential falling below the resting potential) due to the potassium channels remaining open for a short time. Action potentials are self-propagating, and, in the case of efference, travel from the brain, along nerve axons, to muscle cells.

Skeletal muscle fibres (muscle cells are usually called fibres due to their long, thin shape) extend in parallel between the tendons, which attach the muscle to the skeleton. Each muscle fibre is innervated by one efferent motor neuron, while each motor neuron innervates many muscle fibres. The efferent nerve axons (motor neurons) that innervate the muscle divide into many terminal buttons, each of which forms a neuromuscular junction with a muscle fibre at a location referred to as the end-plate. One motor neuron and all the muscle fibres that it innervates comprise a motor unit (MU) -- the smallest voluntarily contractile unit of muscle. When a motor neuron is stimulated, an action potential travels to all the muscle fibres of its motor unit. Each of these muscle fibres is then stimulated, and generates its own single fibre action potential (SFAP) and contractile force. Due to the varying distances from the motor neuron to each muscle fibre, the SFAPs of a single MU are not precisely simultaneous, but they are synchronized, as they are all generated from the same efferent signal. The result of the synchronous firing of all the SFAPs of a given MU is a summated signal called a motor unit action potential

(MUAP). Each MU produces a unique and consistent (i.e., always having the same morphology for a given measuring technique) MUAP.

The morphology of the MUAP is dependent upon the physical structure of the muscle from which it is generated and the manner in which it is measured. Under pathological conditions some of the physical properties of muscle become altered and consequently affect the MUAP. Muscle diseases are numerous, but two broad categories of disorders can be identified: myopathies and neuropathies. Myopathic disorders directly disable muscle fibres, while neuropathies damage motor neurons and the debilitating effect on the muscle fibres is secondary.

In 1954, Buchthal et al. [2] characterized the electrical response of muscle by the mean values of duration, amplitude, and shape of MUAPs. The quantification of shape was by the number of deflections across the base line; MUAP shape thus being described as monophasic, biphasic, triphasic, tetraphasic, or polyphasic. Other characterizations of the MUAP, such as area, amplitude:area ratio, and number of turns (similar to phases, but including all turns, not just those that cross the baseline) have also been used [3]. Various combinations of Buchthal's and others' parameters have proven to be effective for pathological classification, as well as being easy to measure and quantify.

In a study to separate myopathic from neuropathic cases of muscle wasting and weakness, Buchthal showed strong correlation between increased mean duration and/or increased polyphasic activity and several types of muscular dystrophy [4]. Continuing work from these results, Kopec [5] used the Buchthal parameters to characterize myopathy, neuropathy, and motor neuron disease. For each case the analysis was done on four groups of muscles: biceps, quadriceps, interosseus, and tibialis. In the myopathic cases the mean duration and mean amplitude decreased, while the polyphasic activity increased. Patients with motor neuron disease showed increases in mean duration, amplitude and the number of polyphasic MUAPs. Finally, an increase in both mean duration and polyphasic activity was shown to be significant in cases of peripheral neuropathy. Most recently, Stewart et al. [6] have studied the effectiveness of all the above MUAP characteristics, with reference to automatic analysis of neuropathy and myopathy. The findings showed the turns count and area:amplitude ratio to be useful, and concluded that quantitative MUAP analysis may be particularly useful in studying the progression of nerve and muscle diseases.

*Electromyography*

Electromyography is the study of the electrical signals of skeletal muscle, and in a clinical setting the signal is referred to as the electromyogram (EMG). EMG studies are done in several ways, for several purposes. In nerve conduction studies, EMG involves stimulation of a nerve with an electrical impulse, and measurement of the corresponding MUAP at the muscle. Most EMG studies though are done using voluntary contraction, instead of electrical stimulation. Of these studies, two general measurement methods are used: needle electrode and surface electrode.

Needle electrodes are used to measure from a single or a small number of motor units. The needles can be either monopolar or bipolar (concentric), and are often coated with Teflon, except at the tip, to provide a highly localized measurement. It has been generally accepted, and well noted that the measurement of individual MUAPs via needle electrode is the necessary procedure for the diagnosis of or following the progression of neuromuscular disorders [7,8,3].

The assessment of needle electrode signals is often purely qualitative. The signal is displayed on an oscilloscope and simultaneously transmitted through a loudspeaker [7]. An electromyographer is trained to identify various characteristic wave forms by the sounds they generate; however, interpreting these sounds and forming a diagnosis requires a great deal of experience. Therefore, this qualitative assessment is not easily standardized or transferable.

Procedures have been developed for quantifying the needle EMG; however, the primary problem with quantification systems is the overlap of the activity from different MUAPs. Some quantification techniques avoid this problem entirely, by performing what shall be defined as "gross" data processing. That is, no attempt is made to isolate the MUAPs. Instead, the features of the raw signal or of the power spectrum, are calculated and quantified. Willison's method, based on turns count and amplitude recording, was developed in 1964 [9]. Since then, zero-crossing, mean and median frequency, and the integrated signal have been correlated to various neuromuscular disorders [3]. Some

success has been found with gross methods, but the advantage of using the needle is lost because the individual MUAPs are not examined.

As opposed to gross data processing, "decomposition" methods attempt to extract and analyze individual MUAPs. As mentioned earlier, the MUAP is the most fundamental piece of EMG data, and, therefore, has the best potential as a diagnostic tool. Because the needle EMG yields motor unit action potential trains (MUAPTs) decomposition is usually done by detecting and isolating single MUAPs. The simplest systems produce hard-copies of the raw wave form, and MUAPs are identified visually. This type of manual identification of MUAPs is very slow, and is not highly effective because it can be difficult to identify individual MUAPs from raw data. More efficient MUAP identification can be done with computerized systems.

One such system was described and validated in 1985, by K.C.McGill [10]. ADEMG (Automatic Decomposition EMG), as it was named, is a computer program that can isolate up to 15 simultaneously active MUAPs, through the use of either a first or second order difference equation. This accentuates the MUAPs and allows two close spikes to be distinguished. McGill's system also includes an algorithm to characterize and classify MUAPs, and, as noted, there is a great deal of information available relating MUAPs to neuromuscular disorders [5,10,11]. ADEMG, however, makes no attempt to separate superimposed MUAPs and, therefore, is effective only for contractions up to about 30% maximum voluntary contraction (MVC), when the degree of interference between different MUAPs becomes significant. This illuminates a serious limitation to the decomposition of needle EMG. The number of MUs recruited at a given point in time is dependent upon the level of contraction. It is not until about 75% MVC that nearly all the MUs are firing [12] at which point degree of interference is very high. Therefore, performing EMG tests at low levels of contraction will limit interference, but will also limit the scope of the data (i.e. reflecting information from fewer MUs).

Aside from the limited recruitment problem, needle EMG also reflects a limited number of SFAPs at a given time. A needle electrode will only pick up action potentials from muscle fibres lying within about 1mm of the needle tip [13]. This will likely only include 4 or 5 muscles fibres from a given MU. Therefore, if a MUAP is measured using an indwelling electrode, its shape is highly dependent upon the position of the electrode with respect to the muscle fibres, as the fibres nearer to the electrode will have a much

greater effect on the measured signal than the more distant fibres. Slight variations in the electrode placement result in great variation in the MUAP shape. The effective measuring radius of a concentric tip needle electrode is less than 1mm, while the cross sectional radius of the region of muscle containing all the fibres of a particular MU is 5-10mm [14]. Therefore, the MUAP measured from a needle electrode reflects less than $1/25^{th}$ to $1/100^{th}$ of a given MU's muscle fibres. As a consequence, a thorough needle EMG examination may involve as many as twenty needle insertions.

This high degree of invasiveness means that a specialist is required to conduct the test (as proper needle insertion is critical both for the validity of the test and the safety of the patient), and needle EMG is painful for the patient and traumatic to the muscle. This is an especially significant drawback when the EMG tests are to be repeated regularly to help track the progression of a disease. A non-invasive EMG procedure, which can be performed by a non-specialist with computerized data processing, will allow for an efficient and standardized EMG, and less discomfort for patients.

*The Surface EMG*

Electromyographic data can be measured non-invasively from the surface of the skin. The resulting signal is the surface electromyogram, herein referred to a the SEMG. SEMG data aquisition is appealing for the obvious reason that it is non-invasive although it possesses several other positive attributes as well. Its non-invasive, painless nature makes it ideal for following the progression of a disease with repeated examinations. Patients are much more willing to undergo these comfortable examinations regularly, and multiple tests can be performed inexpensively because much less expertise is required for their administration. Another appealing quality of the SEMG is that it measures from a large volume of muscle, as opposed to the needle EMG, which only measures from a small collection of muscle fibres on each insertion. The SEMG also provides a more equal representation of all the muscle fibres of a MU, and, consequently, greatly reduces the variability of the measurement. From the skin surface, all the muscle fibres of a MU are relatively distant, and thereby contribute relatively equally to the surface signal. Small variations in the placement of the surface electrode will not significantly change the

relative distances of the muscle fibres to the electrode, thus not significantly changing the surface motor unit action potential (SMUAP).

If it is fair to say that automatic EMG analysis by means of quantifying MUAP charateristics is a useful procedure, then it is fair to hypothesize that quantifying (SMUAPs) may also be useful for automatic analysis. However, the SMUAP is not a particularly accessible measure. The SEMG measured by a point size monopolar electrode is composed of the superposition of many SMUAPs (of the order of 150 for human brachial biceps -- see chapter 3), thus making it virtually impossible to decompose exactly. A more sophisticated electrode configuration such as a bipolar or spatial filtering multi-electrode, narrows and accentuates the nearer, stronger SMUAPs, thus reducing the amount of interference between SMUAPs [15]. This method has proven useful in extracting SMUAPs directly from the SEMG, but limits the number of SMUAPs contributing to the results. The previously mentioned EMG decomposition system, ADEMG, used with spatial filtering on brachial biceps extracted only five SMUAPs, and was only effective in isolating and extracting them up to 40% maximum voluntary contraction (MVC) [16]. ADEMG makes no attempt to extract information from superimposed SMUAPs, thus reducing the physiologic scope of its results. With the exception of spatial filtering and its limited use then, SEMG analysis is firmly grounded in gross data processing methods, as true decomposition is simply not possible, and the best approaches to SEMG currently lie in power spectral analysis.

A method proposed by Blinowska [17], and further examined by Coatrieux analyzes the power spectrum and relates its features to previously used characteristics of the MUAP[18]. It is shown that from the low frequency spectrum, the mean MU firing rate can be determined, and from the high frequency spectrum the presence of polyphasic SMUAPs can be detected. In a similar study by Paiss and Inbar [19], the SEMG was modelled with autroregressive (AR) parameters. The AR parameters were found to be useful for monitoring muscle fatigue, while the resulting spectrum reflected qualities of the constituent SMUAPs. As above, the low frequency of the spectrum was found to be related to the firing frequency of the MUs, while the high frequency portion was affected by the morphology of the MUAPs. Recently, Priez et al. [20] extended analysis to the power spectrum to include 25 spectral features, including total power, mean and median

frequency, and spectral skewness and kurtosis. These features were then used in a multivariate analysis to identify and index Duchenne muscular dystrophy.

The many power spectrum approaches to SEMG analysis have resulted in various degrees of success and provide various types of information, but they all lack one element: none attempt to characterize the muscle with an action potential, as is done in needle EMG. Ideally, SEMG analysis would combine the broad range of information not easily accessible to needle EMG or the spatially filtered SEMG, while expressing the information in terms of the most fundemental piece of EMG data, tne MUAP.

A novel approach to SEMG analysis was taken by Yana [21], in which he suggested that the SEMG could be modelled as a filtered impulse process. He proposed that if the SEMG is considered to be the sum of many identical elementary wave forms, then such a wave form could be reconstructed from the SEMG using the bispectrum. He considered the SEMG to look like

$$y(t) = \mu \sum_i h(t - \theta_i), \tag{1.1}$$

where $h(t)$ represents the elementary wave form with amplitude $\mu$ and the arrival times of the firing impulses are $\theta_i$s. He then asserted that these times, the $\theta_i$s, form a Poisson process with constant intensity $\lambda$. From this model, the SEMG's power spectrum, $P(e^{j\omega})$, and bispectrum, $B(e^{j\omega_1}, e^{j\omega_2})$, are:

$$P(e^{j\omega}) = \lambda \left| H(e^{j\omega}) \right|^2 \tag{1.2}$$

$$B(e^{j\omega_1}, e^{j\omega_2}) = \lambda H(e^{j\omega_1}) H(e^{j\omega_2}) H^*(e^{j(\omega_1+\omega_2)}), \tag{1.3}$$

where $H(e^{j\omega}) = \mathcal{F}\{h(t)\}$. An inverse solution yielding the magnitude and phase of the elementary wave form was then proposed as:

$$\begin{aligned} \lambda &= P^2(e^{j\omega}) P(e^{j2\omega}) / \left| B(e^{j\omega_1}, e^{j\omega_2}) \right|^2 \\ \left| H(e^{j\omega}) \right| &= \sqrt{P(e^{j\omega})/\lambda} \\ \arg\{H(e^{j\omega})\} &= \sum_{k=1}^{\infty} \frac{1}{2^k} \arg\{B(e^{j2^{k-1}\omega}, e^{j2^{k-1}\omega})\}. \end{aligned} \tag{1.4}$$

In effect, this suggests that the SEMG can be described as a system with a characteristic impulse response. Yana verified his bispectral analysis; however, he did so with a simple and not nearly representative simulation, leaving much work to explore the potential of this method. His model of the SEMG used a crude representation of the SMUAP, but more importantly, did not account for the great number of MUs that contribute to a given signal. This in turn leads to the problem that the many different contributing MUs will not necessarily produce identical SMUAPs. Finally, the bispectral algorithm Yana used was far from optimal and would not have been particularly successful if his simulated SMUAP ("elementary wave form") had not been minimum phase. As will be discussed in chapter 2, a minimum phase impulse response can be resolved from the power spectrum, while recovery of a non-minimum phase response requires a higher order statistical approach. Yana's simulation, therefore, showed little about the effectiveness of the bispectrum; however, his idea of extracting action potential-like information became the primary motivation behind this thesis.

The mathematical groundwork for being able to extract action potential-like information is developed in chapter 2. This groundwork involves the development of a deconvolution procedure that has the ability to estimate a non-minimum phase system impulse response. The end result is a procedure called bicepstral deconvolution. With the understanding of this signal processing tool, a model of the SEMG is developed in chapter 3. This model is developed for two purposes: to synthesized SEMGs and to analyze them using bicepstral deconvolution. The key point of the modelling for analysis is that the SEMG can be characterized by a single action potential referred to as the "representative surface motor unit action potential" (RSMUAP). Chapter 4 contains the methods and their results of five experiments designed to investigate the suitability of the RSMUAP for characterizing the SEMG. The discussion of the results of these experiments, an assessment of the RSMUAP as a tool for SEMG analysis, and a look to future research possibilities are included in the final chapter.

# Chapter 2
# Non-Minimum Phase Deconvolution

*Introduction*

System or impulse response identification is a well known process applicable to the models of many biological systems. As explained in the forthcoming chapter 3, it is reasonable to describe the SEMG as the output of a single input - single output, linear and time-invariant (LTI) system. As a block diagram, the simplified problem looks like:

$$u(n) \longrightarrow \boxed{h(n)} \longrightarrow y(n)$$

**Figure 2.1** The system block diagram. The output, $y(n)$, is equal to the linear convolution of the input, $u(n)$, and the impulse response, $h(n)$.

or, algebraically as $y(n) = h(n) * u(n)$, where $*$ is the linear convolution operator. In the z or Fourier domain this input-output relationship simplifies into a multiplication,

$$Y(z) = U(z) \cdot H(z). \tag{2.1}$$

The system, defined above by an impulse response, is then described by a transfer function,

$$H(z) = Z\{h(n)\} = \sum_{n=-\infty}^{\infty} h(n) \cdot z^{-n} \tag{2.2}$$

or, similarly in the Fourier domain as,

$$H(e^{j\omega}) = F\{h(n)\} = \sum_{n=-\infty}^{\infty} h(n) \cdot \exp(-j\omega n). \tag{2.3}$$

The goal in this thesis is to determine the transfer function $H(z)$ and/or impulse response $h(n)$, given $y(n)$ and no specific knowledge of $h(n)$. This process is called deconvolution.

Some restrictions, however, must be made on both $u(n)$ and $h(n)$. It is assumed that $h(n)$ is deterministic while $u(n)$ results from a stochastic process. That is, the value of $h(n)$ at every index $n$ is fixed, while the value of $u(n)$ at every value of $n$ represents a

random variable, each of which obeys some probability density function (p.d.f.). Knowing that the input to the above system is a random signal, despite that $h(n)$ is deterministic, the output $y(n)$ must also be a random signal. The signal processing of random signals is an extremely involved topic that many entire books attempt to explain, but, in this thesis, only a brief grounding is necessary to understand the methods used to deconvolve $h(n)$ from $y(n)$.

The most complete description of a stochastic process is given by the p.d.f. of all of its random variables [22]. In this thesis no assumptions are made about the mathematical form of the p.d.f.s governing either $u(n)$ or $y(n)$, only that both generate stationary, non-Gaussian signals and that $u(n)$ is white. Assuming that a random signal is stationary implies that the p.d.f.s of all its random variables are identical, and therefore, one p.d.f. can be used to describe the entire signal. Following from that, the first objective of analyzing the random signal $y(n)$ is to gain information about the p.d.f. by which it is governed.

Probability density functions are often described by expected values of the random variable(s) they govern. For example, the mean value of a random variable is the value that one most expects the random variable to be. $\mathrm{E}\{\bullet\}$ is the expectation operator and is defined for a discrete random variable $z$ by

$$\mathrm{E}\{z\} = \sum_{z} z \cdot p(z), \tag{2.4}$$

where $p(z)$ is the p.d.f. for $z$. Without knowing or assuming the mathematical form of the p.d.f., as is the case in this thesis, this definition of expected value cannot be employed directly, and must be replaced by non-parametric estimation methods. The issue of these estimation methodologies is, for the most part, not discussed in this thesis. In many cases, estimates of moments or cumulants are used to describe the p.d.f..

*Moments and Cumulants*

Random signals are commonly described in terms of moments which can be defined in terms of a moment generating function. Given a random signal, $x(n)$, its

moment generating function is defined as [22],

$$M_x(\theta) \equiv \mathrm{E}\{\exp[\theta x]\}. \tag{2.5}$$

The $r$th moment of $x(n)$ is then defined as the $r$th derivative of the moment generating function with respect to $\theta$, evaluated at $\theta$ equals zero; therefore the $r$th moment is

$$m_x^r \equiv \frac{\partial^r M_x(\theta)}{\partial\theta^r}\Big|_{\theta=0} = \frac{\partial^r}{\partial\theta^r}\mathrm{E}\{\exp[\theta\cdot x(n)]\}\Big|_{\theta=0}. \tag{2.6}$$

Moving the differentiation process inside the expectation operator yields the univariate moments of $x(n)$,

$$m_x^r = \mathrm{E}\left\{\frac{\partial^r}{\partial\theta^r}\exp[\theta\cdot x(n)]\right\}\Big|_{\theta=0} = \mathrm{E}\{x^r(n)\cdot\exp[\theta\cdot x(n)]\}\Big|_{\theta=0} \tag{2.7}$$

$$\therefore m_x^r = \mathrm{E}\{x^r(n)\} \tag{2.8}$$

Extending this definition to multivariate moments results in

$$m^r_{x_1,x_2,\ldots,x_k} = \mathrm{E}\{x_1^{r_1}\cdot x_2^{r_2}\cdot\ldots\cdot x_k^{r_k}\}, \tag{2.9}$$

where $r = r_1 + r_2 + \ldots + r_k$. The ensemble of $k$ stochastic processes may represent a single time series with $k$ index spaces, in which case it is common to define the number of index spaces equal to the order of the moment sequence to be calculated. In such a case, an $r$th order, $r$ variate moment sequence of the time series $x(n)$ is defined as

$$m_x(n_1, n_2, \cdots, n_r) = \mathrm{E}\{x(n_1)\cdot x(n_2)\cdot\ldots\cdot x(n_r)\}, \tag{2.10}$$

where the superscript indicating the moment order is dropped because the order is also defined by the order of the index space of $m_x(n_1,\cdots,n_r)$. For sequences stationary up to order $r$, the moment sequence can be written in terms of lags instead of absolute sequence indexes, and if the first index is arbitrarily set to zero, an $r$th order moment sequence is described in $r$-1 space by

$$m_x(l_1,\cdots,l_{r-1}) \equiv m_x(0,l_1,\cdots,l_{r-1}) = \mathrm{E}\{x(n)\cdot x(n-l_1)\cdot\ldots\cdot x(n-l_{r-1})\}. \tag{2.11}$$

Closely related to moments and moment sequences are cumulants, which, strictly speaking, are used to define most spectra, including the power spectrum and bispectrum as well [23]. Taking the logarithm of the moment generating function defined in (2.5), yields

$$C_x(\theta) \equiv \log[M_x(\theta)] = \log[\mathrm{E}\{\exp[\theta x]\}] \tag{2.12}$$

which is the cumulant generating function [24]. Analogously to the moments, the $r$th cumulant of $x(n)$ is defined as the $r$th order derivative of the cumulant generating function evaluated at $\theta$ equals zero. From this point, cumulants are most easily determined in terms of moments. Given (2.12),

$$M_x(\theta) = \exp[C_x(\theta)] \tag{2.13}$$

Then differentiating to calculate the moments yields,

$$m_x^1 = \frac{\partial M_x(\theta)}{\partial \theta}\Big|_{\theta=0} = \frac{\partial \exp[C_x(\theta)]}{\partial \theta}\Big|_{\theta=0} = M_x(\theta)\cdot c_x^1\big|_{\theta=0}. \tag{2.14}$$

Clearly,

$$M_x(\theta)\big|_{\theta=0} = 1, \tag{2.15}$$

and hence,

$$c_x^1 = m_x^1. \tag{2.16}$$

Continuing this process, the relationship between cumulants and moments can be determined for all orders. For orders up to four, the relationships are:

$$\begin{aligned} c^2 &= m^2 - (m^1)^2 \\ c^3 &= m^3 - 3m^2m^1 + 2(m^1)^2 \\ c^4 &= m^4 - 4m^3m^1 - 3(m^2)^2 + 12m^2(m^1)^2 - 6(m^1)^4. \end{aligned} \tag{2.17}$$

Despite that calculating cumulants appears to be an arduous task, for zero mean sequences ($m^1 = 0$) the cumulant sequences of order less than four simply reduce to being equal to the moment sequence of the same order. Therefore, unless otherwise specified, all moments in this thesis are defined as being about the mean, which is achieved by subtracting the mean from the segment of data used to estimate the moments, or more simply, considering all the data to be zero mean. So, although cumulant sequences are alien to many, they can often be replaced with moment sequences, which are relatively common in signal processing. In fact, a second order moment sequence is exactly equal to the well known autocovariance sequence,

$$c_x(l) = \mathrm{E}\{x(k) \cdot x(k+l)\}, \tag{2.18}$$

upon which most spectral methods of stochastic signal processing are based.

The power spectrum of $x(n)$, can be defined as

$$S(e^{j\omega}) = X(e^{j\omega}) \cdot X^*(e^{j\omega}) = \left|X(e^{j\omega})\right|^2 \tag{2.19}$$

where,

$$X(e^{j\omega}) = \sum_{n=0}^{N} x(n) \cdot e^{-j\omega n}. \tag{2.20}$$

One method of estimating the power spectrum of a stochastic process is to Fourier transform its second order cumulant sequence, which as mentioned above, is simply the autocovariance sequence.

The problem with the autocovariance sequence and corresponding power spectrum is that some of the information of the original signal is lost in their estimation. More particularly, only the magnitude, not the phase of the frequency domain of the signal is retained during a power spectrum estimation. The loss of phase information means that, in general, the estimation of the power spectrum is not an invertible process. Every unique power spectrum does not produce a unique time domain sequence, so estimating a time-domain sequence from a power spectrum requires applying constraints to the characteristics of the time-domain signal.

In order to demonstrate that the power spectrum is generally non-invertible, the relationship between the magnitude and phase of a frequency response must be investigated. This can be done rigorously using the derivation of the Hilbert transform, but a simpler, intuitive exploration is more suitable here.

A power spectrum can be represented as a rational function of poles and zeros,

$$\left|H(e^{j\omega})\right|^2 = H(e^{j\omega}) \cdot H^*(e^{j\omega}) = H(e^{j\omega}) \cdot H(e^{-j\omega}) \tag{2.21}$$

$$\left|H(e^{j\omega})\right|^2 = \frac{M\prod_i (1 - c_i e^{j\omega})(1 - c_i^* e^{-j\omega})}{\prod_k (1 - d_k e^{j\omega})(1 - d_k^* e^{-j\omega})}. \tag{2.22}$$

For real valued polynomial coefficients in $H(e^{j\omega})$, poles and zeros exist in complex conjugate pairs, and therefore it is unnecessary to apply the conjugation to the pole and zero locations $d_k$ and $c_i$. These poles and zeros can be plotted in the complex plane if the substitution $z = e^{j\omega}$ is made:

$$|H(z)|^2 = H(z) \cdot H(z^{-1}) = \frac{M \prod_i (1 - c_i z)(1 - c_i z^{-1})}{\prod_k (1 - d_k z)(1 - d_k z^{-1})}. \tag{2.23}$$

From the above relation, it is clear that for every pole at $d_k$ there is a pole at $d_k^{-1}$, and likewise the zeros exist at $c_i$ and $c_i^{-1}$. In terms of the z plane, this means that for every pole or zero inside the unit circle, there is a corresponding pole or zero outside the circle. If $H(z)$ is assumed to represent a stable system, then all its poles lie inside the unit circle. Therefore, the poles outside the unit circle can be inferred to belong to $H(z^{-1})$, and hence, the poles of $H(z)$ can be determined exactly from the power spectrum.

The zeros of a stable sequence, however, are not bound by the restriction of lying within the unit circle. So, every pair of zeros, $c_i$ and $c_i^{-1}$, increases the possible interpretations of the zeros of $|H(z)|^2$ by a power of two. It is clear then, that a sequence cannot be reconstructed from its power spectrum unless restrictions are placed upon its zeros. The most common restriction is to limit the zeros to lie within the unit circle: a sequence having zeros only within the unit circle is referred to as being *minimum-phase* [25].

Therefore, a deconvolution filter that first estimates the autocovariance sequences from the random signal $y(n)$ is limited to estimating a phase restricted, most commonly a minimum phase, system impulse response, $h(n)$. If this limitation is to be avoided, the random signal $y(n)$ must be processed using a method that preserves phase information. Phase information can be retained if, instead of computing the second-order cumulant sequence (i.e., the autocovariance sequence), a higher order cumulant sequence is computed. Transforms of cumulant sequences of order higher than two are sometimes

referred to as higher order spectra [23]. These higher order spectra possess qualities advantageous to solving the deconvolution problem encountered in this thesis.

*The Bispectrum*

Higher order spectra are, simply put, the Fourier transforms of higher order cumulant sequences. While the power spectrum results from the Fourier transform of a second order cumulant sequence,

$$S(e^{j\omega}) = \sum_{l=-\infty}^{\infty} c_x(l) \cdot e^{-j\omega l}, \tag{2.24}$$

the Fourier transform of a third order cumulant sequence is called the bispectrum [23],

$$B(e^{j\omega_1}, e^{j\omega_2}) \equiv \sum_{l_1=-\infty}^{+\infty} \sum_{l_2=-\infty}^{+\infty} c(l_1, l_2) \cdot e^{-j\omega_1 l_1} \cdot e^{-j\omega_2 l_2}, \tag{2.25}$$

and is the first higher order spectrum. Fourier transforms of still higher order cumulant sequences produce correspondingly higher order spectra, but only the bispectrum is used in this thesis, and therefore discussion of the properties of higher order spectra is made herein with respect to the bispectrum. The most natural explanation of the bispectrum is done in the context of, and as an extension of the power spectrum. For this reason, a brief analytical development of the power spectrum follows, and serves as a basis for exploring the bispectrum.

In order to develop a basis for the investigation of the bispectrum, the relationship between the autocovariance sequence and the power spectrum is explored. For the sake of proving (2.24), consider three sequences, $x_1(n)$, $x_2(n)$ and $x_3(n)$ with Fourier transforms $X_1(e^{j\omega})$, $X_2(e^{j\omega})$ and $X_3(e^{j\omega})$. If

$$x_3(l) = \sum_{k=-\infty}^{\infty} x_1(k) \cdot x_2(k+l), \tag{2.26}$$

then

$$X_3(e^{j\omega}) = \sum_{l=-\infty}^{\infty} \left[ \sum_{k=-\infty}^{\infty} x_1(k) \cdot x_2(k+l) \right] e^{-j\omega l}, \tag{2.27}$$

and by changing the order of summation, one gets

$$X_3(e^{j\omega}) = \sum_{k=-\infty}^{\infty} x_1(k) \sum_{l=-\infty}^{\infty} x_2(k+l) \cdot e^{-j\omega l}. \tag{2.28}$$

Making the substitution, $m = k + l$, (2.28) becomes

$$\begin{aligned} X_3(e^{j\omega}) &= \sum_{k=-\infty}^{\infty} x_1(k) \sum_{m=-\infty}^{\infty} x_2(m) \cdot e^{-j\omega(m-k)} \\ &= \sum_{k=-\infty}^{\infty} x_1(k) \cdot e^{-j(-\omega)k} \sum_{m=-\infty}^{\infty} x_2(m) \cdot e^{-j\omega m} \end{aligned}, \tag{2.29}$$

which is simply two Fourier transforms, or

$$\begin{aligned} X_3(e^{j\omega}) &= X_1(e^{-j\omega}) \cdot X_2(e^{j\omega}) \\ &= X_1^*(e^{j\omega}) \cdot X_2(e^{j\omega}) \end{aligned}. \tag{2.30}$$

Therefore, if $x_1(n)$ and $x_2(n)$ are both simply $x(n)$, then $x_3(n)$ is the autocovariance of $x(n)$, and its Fourier transform, $X_3(e^{j\omega})$, is the power spectrum of $x(n)$.

By analogy, the meaning of the Fourier transform of a third order cumulant sequence can be determined. Consider again, three sequences $x_1(n)$, $x_2(n)$ and $x_3(n)$ with Fourier transforms $X_1(e^{j\omega})$, $X_2(e^{j\omega})$ and $X_3(e^{j\omega})$. This time, define a fourth sequence $x_4(l_1, l_2)$ such that

$$x_4(l_1, l_2) = \sum_{k=-\infty}^{\infty} x_1(k) \cdot x_2(k+l_1) \cdot x_3(k+l_2). \tag{2.31}$$

Taking the two dimensional Fourier transform of this equation yields

$$X_4(e^{j\omega_1}, e^{j\omega_2}) = \sum_{l_2=-\infty}^{\infty} \sum_{l_1=-\infty}^{\infty} \left[ \sum_{k=-\infty}^{\infty} x_1(k) \cdot x_2(k+l_1) \cdot x_3(k+l_2) \right] \cdot e^{-j\omega_1 l_1} \cdot e^{-j\omega_2 l_2}, \tag{2.32}$$

which can be re-written as

$$X_4(e^{j\omega_1}, e^{j\omega_2}) = \sum_{k=-\infty}^{\infty} x_1(k) \sum_{l_1=-\infty}^{\infty} x_2(k+l_1) \cdot e^{-j\omega_1 l_1} \sum_{l_2=-\infty}^{\infty} x_3(k+l_2) \cdot e^{-j\omega_2 l_2}. \tag{2.33}$$

Making the substitutions, $p = k + l_1$ and $q = k + l_2$, (2.33) becomes

$$
\begin{aligned}
X_4\left(e^{j\omega_1}, e^{j\omega_2}\right) &= \sum_{k=-\infty}^{\infty} x_1(k) \sum_{p=-\infty}^{\infty} x_2(p) \cdot e^{-j\omega_1(p-k)} \sum_{q=-\infty}^{\infty} x_3(q) \cdot e^{-j\omega_2(q-k)} \\
&= \sum_{k=-\infty}^{\infty} x_1(k) \cdot e^{-j(-\omega_1)k} \cdot e^{-j(-\omega_2)k} \sum_{p=-\infty}^{\infty} x_2(p) \cdot e^{-j\omega_1 p} \sum_{q=-\infty}^{\infty} x_3(q) \cdot e^{-j\omega_2 q}, \quad (2.34) \\
&= \sum_{k=-\infty}^{\infty} x_1(k) \cdot e^{-j(-\omega_1-\omega_2)k} \sum_{p=-\infty}^{\infty} x_2(p) \cdot e^{-j\omega_1 p} \sum_{q=-\infty}^{\infty} x_3(q) \cdot e^{-j\omega_2 q}
\end{aligned}
$$

which is simply three Fourier transforms, or

$$
\begin{aligned}
X_4\left(e^{j\omega_1}, e^{j\omega_2}\right) &= X_1\left(e^{-j(\omega_1+\omega_2)}\right) \cdot X_2\left(e^{j\omega_1}\right) \cdot X_3\left(e^{j\omega_2}\right) \\
&= X_1^*\left(e^{j(\omega_1+\omega_2)}\right) \cdot X_2\left(e^{j\omega_1}\right) \cdot X_3\left(e^{j\omega_2}\right).
\end{aligned} \quad (2.35)
$$

Therefore, using

$$
c_x(l_1, l_2) = \frac{1}{N} \sum_{n=s_1}^{s_2} x(n) \cdot x(n+l_1) \cdot x(n+l_2) \quad (2.36)
$$

as an estimate of the third order cumulants, where

$$
\begin{aligned}
s_1 &= \max[0, N-l_1, N-l_2] \\
s_2 &= \min[N, N-l_1, N-l_2]
\end{aligned}, \quad (2.37)
$$

and setting $x_1(n)$, $x_2(n)$ and $x_3(n)$ equal to $x(n)$, $x_4(l_1, l_2)$ becomes an estimate of the third order cumulant sequence of $x(n)$, and its Fourier transform, by definition, is the bispectrum:

$$
B_x\left(e^{j\omega_1}, e^{j\omega_2}\right) = X^*\left(e^{j(\omega_1+\omega_2)}\right) \cdot X\left(e^{j\omega_1}\right) \cdot X\left(e^{j\omega_2}\right). \quad (2.38)
$$

Decomposition of both $B_x\left(e^{j\omega_1}, e^{j\omega_2}\right)$ and $X\left(e^{j\omega}\right)$ into magnitude and phase components yields

$$
\begin{aligned}
B_x\left(e^{j\omega_1}, e^{j\omega_2}\right) &= \left|B_x\left(e^{j\omega_1}, e^{j\omega_2}\right)\right| \cdot \exp\left[j\Psi_x\left(e^{j\omega_1}, e^{j\omega_2}\right)\right] \\
X\left(e^{j\omega}\right) &= \left|X\left(e^{j\omega}\right)\right| \cdot \exp\left[j\Phi\left(e^{j\omega}\right)\right].
\end{aligned} \quad (2.39)
$$

Then from (2.38) and (2.39) comes,

$$\begin{aligned} \left|B_x\left(e^{j\omega_1}, e^{j\omega_2}\right)\right| &= \left|X\left(e^{j\omega_1}\right)\right| \cdot \left|X\left(e^{j\omega_2}\right)\right| \cdot \left|X\left(e^{j(\omega_1+\omega_2)}\right)\right| \\ \Psi_x\left(e^{j\omega_1}, e^{j\omega_2}\right) &= \Phi\left(e^{j\omega_1}\right) + \Phi\left(e^{j\omega_2}\right) - \Phi\left(e^{j(\omega_1+\omega_2)}\right). \end{aligned} \tag{2.40}$$

Therefore, it can be seen that the phase $\Psi_x$ at any point $\left(e^{j\omega_1}, e^{j\omega_2}\right)$ is directly related to the phase $\Phi$ at three points $\left(e^{j\omega_1}\right)$, $\left(e^{j\omega_2}\right)$ and $\left(e^{j(\omega_1+\omega_2)}\right)$.

An additional property of higher order spectra, which is of relevance to the processing of noisy signals, is that third order cumulant sequences, and therefore the bispectrum as well, are identically zero for stationary Gaussian signals [23]. This can be seen by first examining the moment generating function of a Gaussian sequence. From (2.4) and (2.5), and given that the p.d.f. of the Gaussian distributed random variable, $z_G$, which has a mean of zero and a standard deviation of $\sigma$, is

$$p(z_G) = \frac{\exp\left[-\frac{1}{2}\cdot\left(z_G/\sigma\right)^2\right]}{\sigma\sqrt{2\pi}}, \tag{2.41}$$

it follows that

$$M_{z_G}(\theta) = \sum_{z_G} \exp\left[\theta z_G\right] \cdot \frac{\exp\left[-\frac{1}{2}\cdot\left(z_G/\sigma\right)^2\right]}{\sigma\sqrt{2\pi}}. \tag{2.42}$$

Some algebraic manipulation results in

$$\begin{aligned} M_{z_G}(\theta) &= \frac{1}{\sigma\sqrt{2\pi}} \sum_{z_G} \exp\left[-\tfrac{1}{2\sigma^2}\cdot\left(z_G{}^2 - 2\sigma^2\theta z_G\right)\right] \\ &= \frac{1}{\sigma\sqrt{2\pi}} \sum_{z_G} \exp\left[-\tfrac{1}{2\sigma^2}\cdot\left(\left(z_G - \sigma^2\theta\right)^2 - \sigma^4\theta^2\right)\right] \\ &= \exp\left[\frac{\sigma^2\theta^2}{2}\right] \sum_{z_G} \frac{1}{\sigma\sqrt{2\pi}} \exp\left[-\frac{\left(z_G - \sigma^2\theta\right)^2}{2\sigma^2}\right]. \end{aligned} \tag{2.43}$$

The summation factor constitutes the integration of a normal p.d.f. over its entire domain, and therefore, is equal to one. Hence (2.43) reduces to

$$M_{z_G}(\theta) = \exp\left[\frac{\sigma^2\theta^2}{2}\right], \tag{2.44}$$

which can be expanded into a power series to get

$$M_{z_G}(\theta) = 1 + \frac{(\sigma\theta)^2}{2} + \frac{(\sigma\theta)^4}{4\cdot 2!} + \frac{(\sigma\theta)^6}{8\cdot 3!} + \cdots. \tag{2.45}$$

Recall here (eq. (2.14)) that moments can be derived from the derivatives of the moment generating function. Clearly from (2.45), $M_{z_G}(\theta)$ has no odd powers of $\theta$, and consequently, all odd order derivatives of $M_{z_G}(\theta)$ are equal to zero when $\theta = 0$. Therefore, from (2.17), the third order cumulant sequence, and in turn from (2.25), the bispectrum of the Gaussian distributed random variable $z_G$ is zero. In fact, further investigation will reveal that while only odd order moments are zero for Gaussian signals, all cumulants of order greater than two are zero for such signals [23]. This is one of the main reasons for defining higher order spectra in terms of cumulants instead of moments. Another important reason for using cumulants instead of moments is that the cumulant generating function is distributive, while the moment generating function is not. This property is self evident from (2.5) and (2.12). In terms of signal processing, this means that if a signal is considered to be the sum of two independent signals, which is the case in the very common additive noise model, then the cumulants of the sum are equal to the sum of the cumulants. If then, one of the two signals is Gaussian, which is a common assumption of noise, then it contributes nothing to the higher order cumulants of the output signal. This makes the bispectrum attractive for studying non-Gaussian signals corrupted with additive Gaussian noise.

A plethora of signal processing methodologies have been extended to take advantage of higher order spectra and their desirable qualities. Homomorphic signal processing has been used with some success to solve the deconvolution problem presented at the beginning of this chapter. Recently, however, the homomorphic approach to deconvolution has been extended to the bispectral domain [26], and it is this deconvolution method that is used is this thesis for SEMG analysis.

*The Homomorphic method* [25,27]

Higher order spectra and random signal processing aside, the deconvolution process itself must be examined. Given the output signal from a system in general, or at least, a signal derived from the output signal, and knowing that it is comprised in some manner of two independent signals, the general goal may be to divide the output signal into its constituent parts. When two or more signals are summed by simple addition, as is the case with additive noise, the principle of superposition makes it possible to separate the non-overlapping signals by filtering with a linear system. With the linear system T below, it is clear that additive signals in the time domain are also additive signals in the transformed domain.

$$\mathrm{T}\{\alpha x_s(n)+\beta x_N(n)\}=\alpha\mathrm{T}\{x_s(n)\}+\beta\mathrm{T}\{x_N(n)\}. \tag{2.46}$$

Signals that are combined through more complicated mechanisms, though, such as convolution, cannot generally be separated with a simple linear filter, if the property of superposition does not hold. However, there exists nonlinear systems that may be defined in terms of algebraically linear transformations between signal domains. Consider $\Diamond$ to represent a rule for combining input signals (e.g., multiplication, convolution, addition, ...), and $\bullet$ represent a rule for combining output signals. Input signals are combined with scalars using $\otimes$, while $\circ$ denotes combination of output signals with scalars. Then a system D, that obeys the relation

$$\begin{aligned}\mathrm{D}\{x_s(n)\Diamond x_N(n)\} &= \mathrm{D}\{x_s(n)\}\bullet\mathrm{D}\{x_N(n)\}\\ &= \hat{x}_s(n)\bullet\hat{x}_N(n)\end{aligned} \tag{2.47}$$

and

$$\mathrm{D}\{\alpha\otimes x(n)\}=\alpha\circ\mathrm{D}\{x(n)\} \tag{2.48}$$

is called a *homomorphic* system. In order to deconvolve signals then, a homomorphic system for convolution must be determined.

It is well known that both the Fourier transform and the z-transform convert a convolution operation into a multiplication; thus, they may be considered homomorphic with convolution as the input operation and multiplication as the output operation. By the same logic, the logarithm operation is homomorphic with multiplication and addition being

the input and output operations respectively. Hence, cascading these two operations will produce a homomorphic system having convolution as the input operation and addition as the output operation. It is often desirable to have the output signal represented as a sequence in $n$ rather than a z-transform, so the inverse z-transform can be appended to this system, since it obeys the conventional rules of superposition. The complete system then becomes

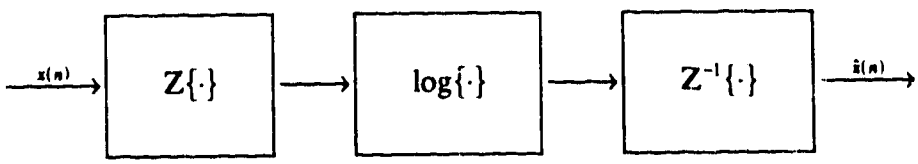


**Figure 2.2** A homomorphic system for deconvolution. The output is referred to as the complex cepstrum.

where the output, $\varsigma_x(n) \equiv \hat{x}(n)$, is defined as the complex cepstrum.

It appears then that homomorphic techniques are applicable to deconvolution problems in general. Relating these methods to the system modelled at the beginning of this chapter in figure 2.1, the complex cepstrum $y(n)$ is

$$\varsigma_y(n) = Z^{-1}\{\log[Z\{y(n)\}]\}, \tag{2.49}$$

and as shown below separates the $h(n)$ and $u(n)$ components of the signal,

$$\begin{aligned} \varsigma_y(n) &= Z^{-1}\{\log[Y(z)]\} \\ &= Z^{-1}\{\log[H(z)U(z)]\} \\ &= Z^{-1}\{\log[H(z)] + \log[U(z)]\} \\ \varsigma_y(n) &= \varsigma_h(n) + \varsigma_u(n) \end{aligned} \tag{2.50}$$

Then, if a linear filter function can be found to separate $\varsigma_h(n)$ and $\varsigma_u(n)$, both $h(n)$ and $u(n)$ can be reconstructed in the discrete time domain:

$$h(n) = Z^{-1}\{\exp[Z\{\varsigma_h(n)\}]\}, \tag{2.51}$$

and likewise for $u(n)$.

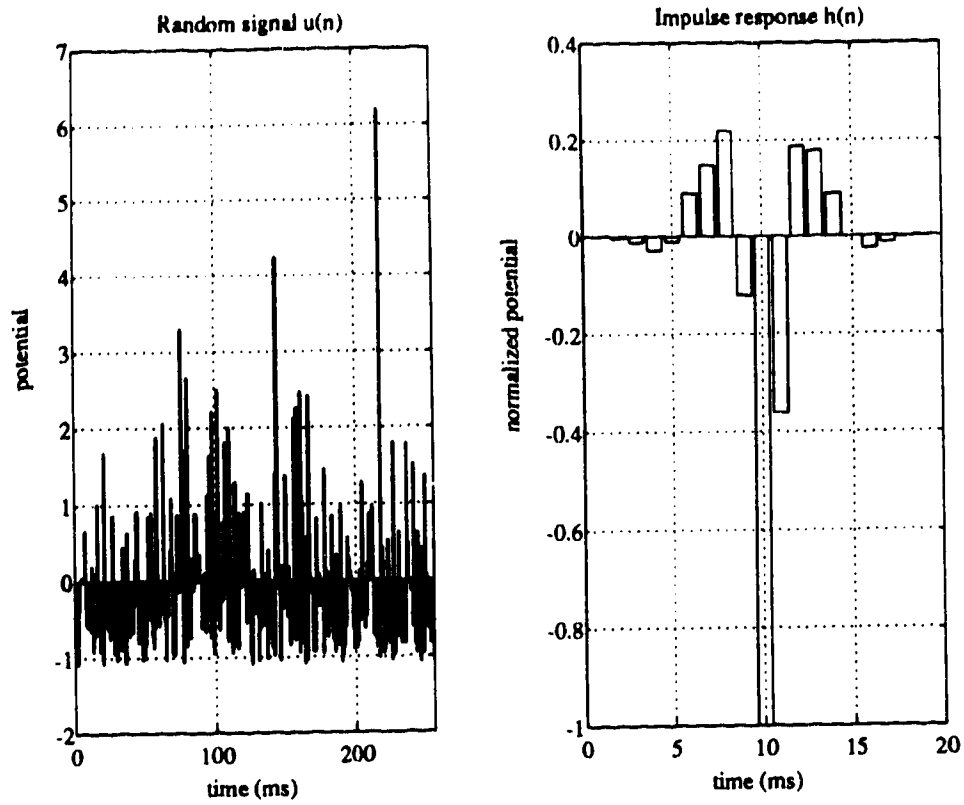


**Figure 2.3** Example signals for homomorphic deconvolution. It is desireable to be able to deconvolve the input signal, $u(n)$, and/or the system impulse response, $h(n)$.

Note that there are no phase restrictions on the solution $h(n)$ (i.e., it is a non-minimum phase reconstruction of the system impulse response); however, the consequence of $u(n)$ being a random signal, once again prevents a simple solution. The existence of a linear filter to separate $\varsigma_h(n)$ and $\varsigma_u(n)$ requires that these two signals do not overlap in the cepstral domain. Shown in figures 2.3 and 2.4 are two time sequences, $h(n)$ and $u(n)$, and their complex cepstra, $\varsigma_h(n)$ and $\varsigma_u(n)$. The signal $h(n)$ represents a typical system impulse response, existing in the low time domain, while $u(n)$ is a zero-mean, exponentially distributed, random white sequence. Clearly both cepstra, $\varsigma_h(n)$ and $\varsigma_u(n)$, occupy the same domain, and if added together, would be impossible to separate. In the case of seismic signal deconvolution, where the complex cepstrum has been used to

reconstruct non-minimum phase solutions, the input signal $u(n)$ is a train of well spaced impulses. In the cepstral domain, such an input also produces a train of well spaced impulses; thus, little interference between the cepstra occurs.

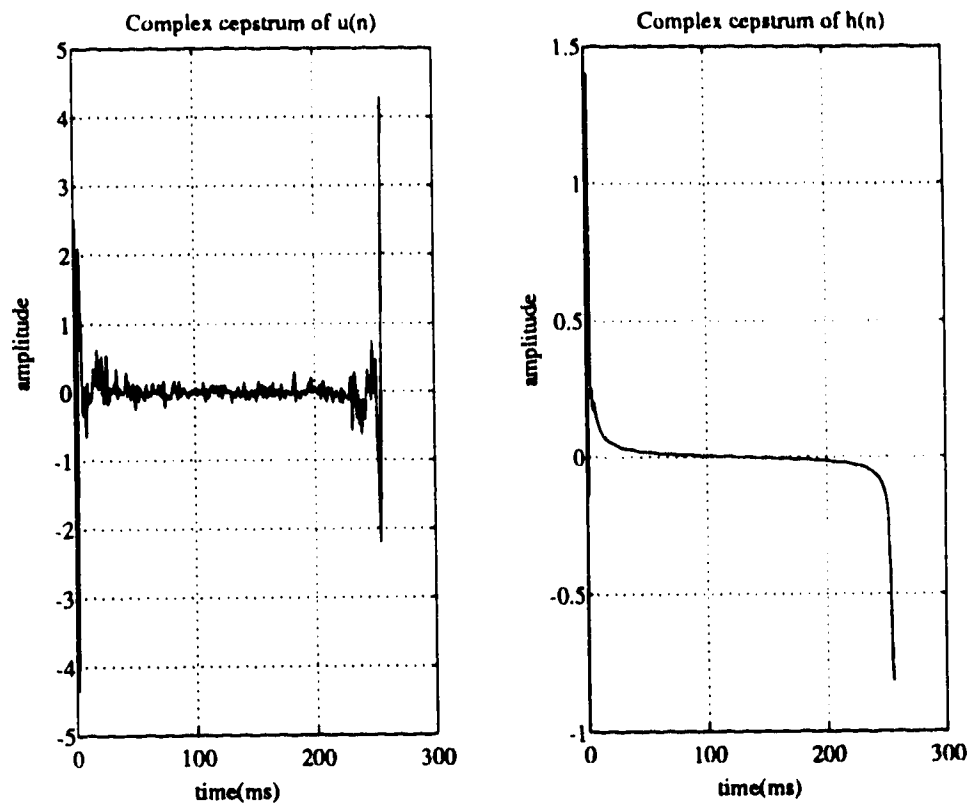


**Figure 2.4** The complex cepstra (real part only shown, imaginary part zero) of example signals. Because both cepstra are significant over the same domain, it is difficult or impossible to extract them seperately from $\varsigma_y(n)$.

For the case where $u(n)$ is a random sequence, cepstral domain interference can be avoided if the complex cepstrum is replaced with the real cepstrum. The difference between these two transforms is that the complex cepstrum uses the complex z-domain signal, while the real cepstrum is defined in terms of the magnitude of the z-domain. That is,

$$\varsigma_y'(n) = Z^{-1}\left\{\log\left[\left|Z\{y(n)\}\right|\right]\right\}. \tag{2.52}$$

The input signal, being uncorrelated, produces a full-band, smooth magnitude spectrum,

and therefore, results in a single impulse at zero in the cepstral domain. Having only one spike interfering with the cepstrum of the impulse response means that separation is not a problem. However, as discussed previously, deconvolution based on the power/magnitude spectrum produces only a minimum phase (or only a maximum phase) solution.

It is shown in the next section (eqs. (2.53) and (2.70)) that a system can be decomposed into its minimum phase and maximum phase components. In order to emphasize the importance of being able to estimate both the minimum and maximum phase components of a system, figure 2.5 shows an impulse response and its minimum and maximum phase components. From the accompanying pole-zero plots it can be seen that the minimum phase component contains zeros and poles inside the unit circle, while the maximum phase component contains zeros outside the unit circle. (It could also contain poles outside the unit circle if the restriction of a stable system is removed.) It seems clear that the mixed phase (or non-minimum phase) impulse response is not well represented in the time domain by either its the minimum of maximum phase components, thereby indicating that if the most informative impulse response is to be estimated, it must be non-minimum phase. A power spectrum based deconvolution procedure can be used to estimate hmn(n) or hmx(n) of figure 2.5, but not both, and consequently, not the non-minimum phase response, h(n). The solution to this problem is, of course, to employ cepstrum based on the bispectrum, which preserves magnitude and phase information, thus allowing for estimation of the non-minimum phase impulse reponse.

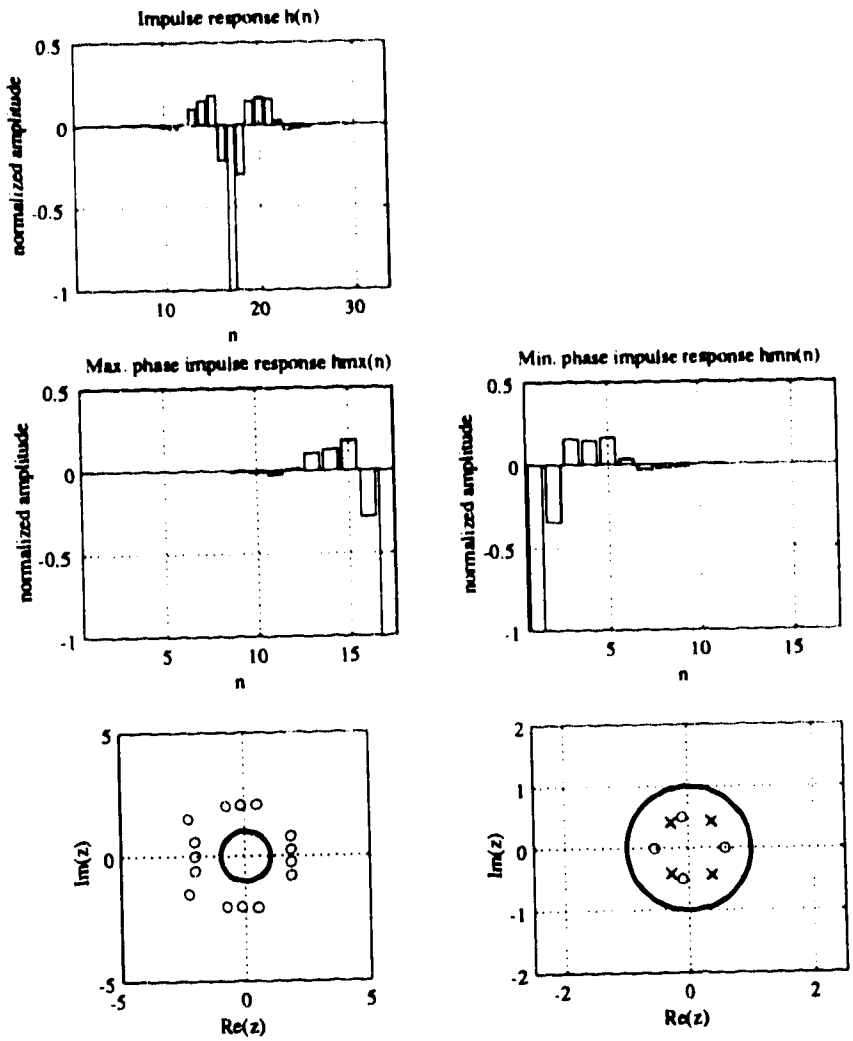


**Figure 2.5** Decomposition of a mixed phase impulse reponse into its minimum phase and maximum phase components. There is another zero of the maximum phase response at z ~= -20 which is not shown. Shown as a point of reference on each pole-zero plot is the unit circle.

*The Bicepstral method* [26]

The idea of applying higher order spectra in conventional signal processing procedures, as mentioned earlier, allows one to benefit from the properties of higher order spectra, while taking advantage of previously developed methodologies. In following

from homomorphic signal processing, which has proven to be effective for some deconvolution problems, a method of deconvolution stemming from the complex logarithm of the bispectrum (heretofore referred to as the bicepstrum) has been developed by Pan and Nikias [26], and is outlined here.

The transfer function $H(z)$, as described previously, being non-minimum phase in general, can be written in terms of minimum and maximum phase components:

$$H(z) = A \cdot z^{-r} \cdot I(z^{-1}) \cdot O(z) \tag{2.53}$$

where

$$I(z^{-1}) = \frac{\prod_{i=1}^{L}(1-a_i z^{-1})}{\prod_{i=1}^{L}(1-c_i z^{-1})} \tag{2.54}$$

is the minimum phase component with poles and zeros inside the unit circle, and

$$O(z) = \prod_{i=1}^{L}(1-b_i z) \tag{2.55}$$

is the maximum phase component with zeros outside the unit circle. Recall that the output signal $y(n)$ is equal to the convolution of the input signal $u(n)$ with the impulse response $h(n)$. So, the bispectrum of $y(n)$ is equal to the bispectrum of $u(n)$ multiplied by the bispectrum of $h(n)$. The latter is, by (2.38), and in the z-domain,

$$B_h(z_1, z_2) = H(z_1)H(z_2)H(z_1^{-1}z_2^{-1}). \tag{2.56}$$

The system input, being a white, non-Gaussian random sequence has a z-transform equal to a constant magnitude and its bispectrum is

$$B_u(z_1, z_2) \equiv \beta. \tag{2.57}$$

In terms of a a third-order cumulant sequence (2.57) translates to an impulse at the origin. As an aside, it can be shown that $\beta$ is proportional to the coefficient of skewness of the signal, which is defined in equation (3.18). It follows from (2.57) then, that the bispectrum of output signal $y(n)$ is

$$B_y(z_1, z_2) = \beta \cdot H(z_1)H(z_2)H(z_1^{-1}z_2^{-1})$$

$$\therefore \tag{2.58}$$

$$B_y(z_1, z_2) = \beta \cdot A \cdot I(z_1^{-1})I(z_2^{-1})I(z_1 z_2) \cdot O(z_1)O(z_2)O(z_1^{-1}z_2^{-1}).$$

Then the bicepstrum of $y(n)$ is defined as

$$\varsigma_y(m,n) \equiv Z^{-1}\left\{\log\left[B_y(z_1, z_2)\right]\right\}$$

$$= Z^{-1}\left\{\begin{array}{l} \log|\beta \cdot A| \\ +\log\left[I(z_1^{-1})\right] + \log\left[I(z_2^{-1})\right] \\ +\log\left[O(z_1)\right] + \log\left[O(z_2)\right] \\ +\log\left[I(z_1 z_2)\right] + \log\left[O(z_1^{-1}z_2^{-1})\right] \end{array}\right\}$$

(2.59)

Using an expansion of the lograrithm to determine the inverse z-transform, the bicepstrum is shown to contain the poles and zeros of the minimum and maximum phase transfer functions:

$$\varsigma_y(m,n) = \begin{cases} \log|\beta \cdot A| & m = 0, n = 0 \\ -\frac{1}{n}A^{(n)} & m = 0, n > 0 \\ -\frac{1}{m}A^{(m)} & n = 0, m > 0 \\ \frac{1}{m}B^{(-m)} & n = 0, m < 0 \\ \frac{1}{n}B^{(-n)} & m = 0, n < 0 \\ \frac{1}{n}B^{(n)} & m = n > 0 \\ \frac{1}{n}A^{(-n)} & m = n < 0 \\ 0 & \text{otherwise} \end{cases}$$

(2.60)

where

$$A^{(k)} \equiv \sum_{i=1}^{L_1} a_i^k - \sum_{i=1}^{L_3} c_i^k$$
$$B^{(k)} \equiv \sum_{i=1}^{L_2} b_i^k \tag{2.61}$$

It has also been shown that the third moment sequence is related to the bicepstrum via

$$\sum_{k=-\infty}^{+\infty} \sum_{l=-\infty}^{+\infty} k\varsigma_y(k,l) c_y(m-k,n-l) = -mc_y(m,n) \tag{2.62}$$

This equation is important because it allows the above relationship between the bicepstrum and the transfer function to be reduced to a relationship between the third moment sequence and the transfer function, thus permitting the complete estimation of the bispectrum to be bypassed. Substituting (2.60) into (2.62), the third order moment sequence of $y(n)$ becomes related to the pole-zero characteristics of the system impulse response $h(n)$, via the so-called *cepstral equation*:

$$\sum_{k=1}^{\infty} \left\{ A^{(k)} \left[ c_y(m-k,n) - c_y(m+k,n+k) \right] + B^{(k)} \left[ c_y(m-k,n-k) - c_y(m+k,n) \right] \right\} = -mc_y(m,n) \tag{2.63}$$

Before this equation can be solved, the infinite summation must be truncated at a manageable point. The bicepstral coefficients $A^{(k)}$ and $B^{(k)}$ have been shown to decay exponentially, which means there exists a finite summation that is a very good approximation to the above infinite sum. Following directly from (2.61), along with (2.54) and (2.55), it can be shown that $A^{(k)}$ and $B^{(k)}$ decay to a magnitude of $C$ in $p$ and $q$ terms, respectively, where

$$p = \frac{\ln[C]}{\ln[a]}, \text{ and } q = \frac{\ln[C]}{\ln[b]}, \tag{2.64}$$

such that

$$\max\left[|a_i|,|c_i|\right] < a < 1$$
$$\max\left[|b_i|\right] < b < 1 \tag{2.65}$$

This means that $p$ and $q$ depend, respectively, on the proximity of the minimum and maximum phase poles and zeros to the unit circle. The closer the nearest pole or zero to the unit circle, the larger $p$ or $q$ will be, and therefore, the more bicepstral coefficients will be required to adequately approximate the infinite sum in the *cepstral equation*. Determining suitable values for $p$ and $q$ can be done using (2.64) and (2.65) and a priori knowledge of the poles and zeros of the system. However, from (2.60), and given that the cepstral components decay exponentially, $p$ and $q$ can be estimated directly from the third order cumulant sequence of $y(n)$. The lag of the furthest significant term from the origin represents the largest value of $k$ in the cepstral equation.

Following the truncation of the infinite sum, (2.63) can be solved using one of two methods. In most cases the most practical solution method forms the cepstral equation into an over determined system of equations, allowing $A^{(k)}$ and $B^{(k)}$ to be solved in a least-squares manner. This method is the most computationally efficient until the truncation points $p$ and $q$ become very large (~80 and above). In these cases more efficient computation of $A^{(k)}$ and $B^{(k)}$ can be achieved using a FFT based solution which follows directly from the convolution (2.62), which relates the bicepstrum to the third order cumulants.

Finally, it has also been shown that $A^{(k)}$ and $B^{(k)}$ are found in the minimum and maximum phase components of the differential cepstrum of the impulse response $h_d(n)$. The differential cepstrum, $h_d(n)$, is defined as

$$h_d(n) \equiv Z^{-1}\left\{\frac{1}{H(z)} \cdot \frac{\partial H(z)}{\partial z}\right\}, \tag{2.66}$$

and is the sum of the differential cepstra of the minimum and maximum phase components of the impulse response:

$$h_d(n) = i_d(n) + o_d(n). \tag{2.67}$$

These components are then related to bicepstral coefficients by

$$i_d(n) = \begin{cases} A^{(n-1)} & n \geq 2 \\ 0 & n \leq 1 \end{cases}$$
$$o_d(n) = \begin{cases} 0 & n \geq 1 \\ -B^{(1-n)} & n \leq 0 \end{cases}, \tag{2.68}$$

which, in turn, are related to the minimum and maximum phase components of the system impulse response by the recursive relations

$$\begin{aligned} i(n) &= \frac{-1}{n} \sum_{k=2}^{n+1} i_d(k) \cdot i(n-k+1), \text{ for } n \geq 1 \\ o(n) &= \frac{-1}{n} \sum_{k=n+1}^{0} o_d(k) \cdot o(n-k+1), \text{ for } n \leq -1. \\ i(0) &= o(0) = 1 \end{aligned} \tag{2.69}$$

The system impulse response, the original objective, is then simply the convolution of its minimum and maximum phase components:

$$h(n) = i(n) * o(n), \tag{2.70}$$

which is evident from the system transfer function having been identified as the multiplication of its minimum and maximum phase components,

$$H(z) = A \cdot z^{-r} \cdot I(z^{-1}) \cdot O(z). \tag{2.71}$$

# Chapter 3
# Modelling

## *Introduction*

In this chapter, two SEMG models are developed. The first model is developed for the purpose of simulating SEMG, and is consequently referred to as the synthesis model. Following from the synthesis model, and in light of the bicepstral method of deconvolution presented in chapter 3, the analysis model is developed.

## *The Synthesis Model*

The synthesis model serves as the basis for simulating the SEMG that will be used to evaluate the method of bicepstral deconvolution. The benefit of using simulated data instead of clinically accumulated data is threefold: ① an unlimited amount of data is available, ② particular neuro-muscular properties can be varied while others are held as controls, and ③ clinical data acquisition variations (electrode type, sampling rate) can be modelled, while practical complications (skin impedance, EM interference, electronic design) can be simplified or ignored. Before a synthesis model is developed to simulate the SEMG, the objectives of the model must be clarified. It is important to remember at this point that the purpose of this work is not to identify or discriminate particular pathological conditions using SEMG, but rather to investigate, from an engineering perspective, a particular method of analysing the SEMG. Meaningful results require a good, but general representation of the SEMG, which in turn requires a quality model of the SMUAP.

The simulations used in this thesis involve three distinct models. As a basis for the simulation of the SEMG, the SMUAP is modelled and simulated. A model previously outlined by McGill [28] is used, with some parameter changes, to simulate healthy SMUAPs. Then, a model describing the effect of disease on the above model is used to simulate the SMUAPs of diseased muscle. Depending on the level of sophistication employed, the effects of many particular neuro-muscular diseases could be

modelled. In this thesis, a model simulating the effects of myopathic disorders in general is employed to evaluate the ability of bicepstral deconvolution to detect the existence of pathology. And, because it is desirable to use SEMG for repeated examinations to follow the progression of disease, this myopathy model is quantized into several stages. Finally, simulated SMUAPs are incorporated into a larger scale model of muscle in order to simulate SEMGs from the superposition of SMUAPs.

For this work, due to availability of data in the literature, all simulated data is based upon the brachial biceps. That choice, and the choice of many of the model's parameters are made somewhat arbitrarily for the sake of expedience, given that the signal processing is the focus of this work. However, the effects of varying some of the modelling parameters are investigated in chapters 4 and 5, with the goal of indicating that the experimental results based on simulated SEMG are not strictly dependent upon this particular sythesis model.

*Modelling Healthy SMUAPs*

A potential measured on the skin surface due to a SFAP can be described as resulting from two tripoles moving in opposite directions away from the endplate of the fibre [28].

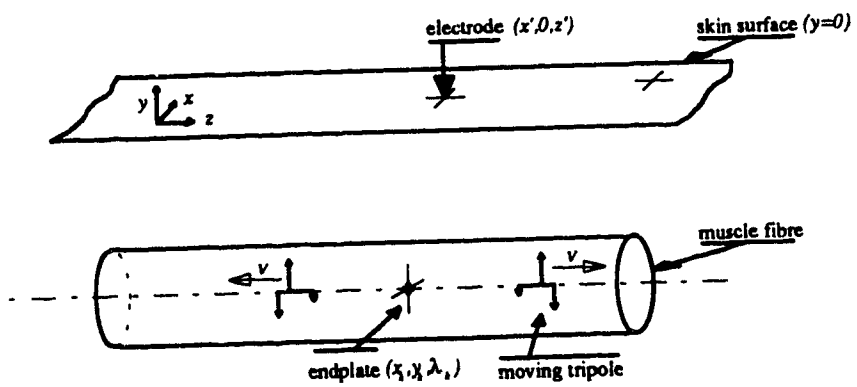


**Figure 3.1** The double tripole model of the surface-measured SFAP (Not to scale). At any point in time, the tripoles are symmetric about the endplate.

With $y = 0$ representing the skin surface and the muscle fibre, centered at $z = 0$, oriented parallel to the $z$ axis, the point of measurement is $(x', 0, z')$, and the location of the end-

plate of fibre $k$ is $(x_k, y_k, \lambda_k)$. The strength of the $i$th pole is $\alpha_i$, and the separation between the leading and the $i$th poles of a tripole is $l_i$, as shown in figure 3.2. The values used by McGill to define the tripoles are shown in the table 3.1.

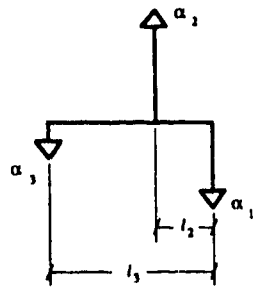


**Figure 3.2** Tripole unit. Each pole $\alpha_i$ is a point current source, and is spatially offset from first pole $\alpha_1$, by $l_i$.

| | $i=1$ | $i=2$ | $i=3$ | $i=4$ | $i=5$ | $i=6$ |
|---|---|---|---|---|---|---|
| $\alpha_i\ (A/m^2)$ | 24.6 | -35.5 | 10.8 | 24.6 | -35.5 | 10.8 |
| $l_i\ (mm)$ | 0.0 | 2.1 | 6.9 | 0.0 | 2.1 | 6.9 |
| $\varepsilon_i$ | +1 | +1 | +1 | -1 | -1 | -1 |

**Table 3.1** Tripole characteristics.

The action potential begins at time $n=0$, when the poles begin moving two at a time in opposite directions from the endplate to the tendons. Each pole moves with conduction velocity $v_k$, which is unique for a given fibre, and the location of the $i$th pole of the $k$th fibre is then

$$z_{ki}(n) = \begin{cases} \lambda_k & \text{if } v_k n < l_i \\ \lambda_k + \varepsilon_i (v_k n - l_i) & \text{if } l_i \le v_k n \le L + l_i - \varepsilon_i \lambda_k, \\ \varepsilon_i L & \text{if } v_k n \ge L + l_i - \varepsilon_i \lambda_k \end{cases} \tag{3.1}$$

where $2L$ is the length from tendon to tendon of the muscle fibre, and $\varepsilon_i$, being +1 or -1, indicates the direction of propagation of the $i$th pole. The SFAP of the $k$th fibre, $\phi_k(n)$,

is then the time domain sum of the potentials resulting from each of the six poles:

$$\phi_k(n) = \frac{a_k^2}{4\pi\sigma} \sum_{i=1}^{6} \frac{\alpha_i}{\sqrt{(x'-x_k)^2 + y_k^2 + (z'-z_{k_i}(n))^2}}, \tag{3.2}$$

where $\sigma$ is the conductivity of the tissue, and $a_k$ is the $k$th fibre's diameter.

Given this model of the surface-measured SFAP, the SMUAP is then described as the sum of all the SFAPs of a given motor unit,

$$\Phi(n) = \sum_{k=1}^{N} \phi_k(n) \tag{3.3}$$

where $N$ equals the number of fibres in the motor unit. In calculating $\Phi(n)$, the number and distribution of fibres and end-plates in a given MU, the tissue conductivity, and the muscle fibres' length, diameter, and conduction velocity must be considered.

The structure of the motor unit is dictated by the size, number, and arrangement of muscle fibres. The length of fibres for human brachial biceps obviously varies from person to person, and in this study is set to a reasonable value of 140mm as was done by McGill in his modelling. Previous needle EMG models have used 55μm as the mean fibre diameter with a standard deviation of 6μm [29,30], while other work has indicated larger mean values of 70μm (64μm for type I fibres and 73μm for type II fibres -- comprising roughly 37% and 63% of the total respectively [31]). The estimates for the number of fibres per motor unit also ranges widely from roughly 150 to 225 [31]. As will be discussed later, the number and size of muscle fibres in a motor unit are used to estimate the distribution of motor units through a cross section of muscle. As a compromise then for assuming that 100% of the muscle cross section is occupied by muscle fibres, the larger of the estimates for muscle fibre size and number of fibres per motor unit are used in the following simulations. That is, a mean fibre diameter of 70μm with standard deviation of 6μm, and 225 fibres per MU are used.

The arrangement of fibres and end-plates are less disputed quantities. It has been shown that the muscle fibres of a MU are distributed uniformly throughout a roughly circular cross section [32], which, in the case of the brachial biceps, is about 5mm in diameter [14]. Thus, there is a great deal of overlap between MUs. In the following simulations the coordinates of a fibre are given relative to the center of the distribution of

the fibres for a given MU. These coordinates $x_c$ and $y_c$ are chosen randomly from a uniform distribution ranging between -2.5mm to +2.5mm, thus resulting in a square distribution of fibres rather than the proposed circular distribution. The placement, in the x-y plane, of the center of the MU must also be determined. This is discussed more in the *SEMG Modelling* section, but simply put now, if the conductivity of the tissue is considered isotropic, then only the net distance, not direction, from the source to the point of measurement is important. This means that all muscle fibres can be considered to be directly beneath the electrode, in the *y-z* plane. Therefore, SMUAPs can be categorized by either depth or distance interchangeably, the symbol $D$ is used here for both. The values $x_k$ and $y_k$ then become

$$\begin{aligned} x_k &= x_c + D \\ y_k &= y_c + D \end{aligned} \tag{3.4}$$

This also means that the conductivity is assumed to be a constant; the value 0.21mho/m is used in the following simulations [33].

Having the x and y coordinates of a muscle fibre, the location of the end-plate along the z axis remains to be determined. In general, the end-plate is situated in the middle of the muscle fibre, thus ensuring the fastest activation of all the fibre's contractile material. In most muscles, the fibres are roughly equal in length and parallel, so the end-plates are distributed across a small region about the middle of the muscle known as the end-plate zone. In human brachial biceps the size of the end-plate zone is 5-10mm wide [31]. Thus, for the following simulations the location of the endplate along the $z$ axis for each fibre of a motor unit, $\lambda_i$, is randomly chosen from a uniform distribution between -5mm and +5mm, where $z = 0$ is the middle of the fibre.

The conduction velocity of the *i*th fibre, $v_i$, represents the most significant alteration to McGill's modelling. Muscles contain a combination of fast and slow conducting fibres, but the mean is usually between 3 and 5m/s; 4.7m/s is one value reported for biceps [34]. Conduction velocity is primarily dependent upon fibre diameter, and in healthy muscle the variation of fibre size is relatively small. Therefore, as was done by McGill, the conduction velocity of healthy muscle may be considered a constant. In this thesis, however, it is desireable to model the effects of myopathy on the SEMG, and the most significant contribution to MUAP change due to disease in general is the

muscle fibre conduction velocity [35]. For the simulations in this thesis, the relationship

$$v_k = 0.711\sqrt{a_k} + 1.3549 \tag{3.5}$$

is used, the reasoning for which is described in the *Modelling Diseased SMUAPs* section. With this relation, the conduction velocity is varied with respect to the square root of the fibre diameter (70μm) and the mean conduction velocity for healthy muscle is roughly 4.6m/s, similar to the previously cited estimate of 4.7m/s.

*Modelling Diseased SMUAPs*

As well as from healthy muscle, SMUAPs from diseased muscle must also be simulated. Considering neuro-muscular diseases from one broad category, myopathies, as mentioned in chapter 1, their effects on the SMUAP model must be considered. A combination of both fibre atrophy and hypertrophy increases the variability of fibre diameter, resulting in the wide but smooth histogram of sizes frequently seen in myopathy [36]. When individual muscle fibres become diseased, they begin to atrophy and consequently loose strength. In response to this loss of strength, still healthy muscle fibres may hypertrophy [36]. As the disorder progresses, more and more muscle fibres become diseased and atrophied, producing a general decrease in fibre size. Muscle fibre atrophy continues until a point when the fibre becomes ineffective. In studies by Stalberg, functioning brachial biceps muscle fibres were found to have a lower bound of roughly 25μm diameter [37].

In modelling the progression of a myopathy, fibre size is very important in determining the SMUAP because both the conduction velocity and the SFAP amplitude are functions of the fibre diameter. In equation (3.2), the amplitude is proportional to $a^2$, similar to the value of $a^{1.7}$ reported by De Luca [38], while equation (3.5), as supported by Plonsey [33], models conduction velocity is roughly proportional to $\sqrt{r}$. In recent needle EMG simulation studies by Nandedkar et al. [29], the conduction velocity of muscle cells was modelled as being proportional to fibre diameter, but it was also noted that this model may have been exaggerating the effect of fibre size on conduction velocity. The square root relationship between fibre radius and conduction velocity was also found to be superior to the linear model in another recent study by Kossev et al. [12].

The basis of the relationship (3.5) between fibre diameter and conduction velocity used here is in the previously mentioned needle EMG simulations by Nandedkar et al.. In these simulations the conduction velocities of 2.2m/s and 5.2m/s are used at fibre diameters of 25μm and 85μm, respectively. Keeping in mind the general purpose of this study, it is assumed that the order of the relationship between fibre diameter and conduction velocity is more important than the particular values of either. Therefore, as a matter of convenience, the relationship between diameter and conduction velocity used in this model was based on the two values above without further justification. Unlike Nandedkar et al., however, a square-root as opposed to a linear relationship is used.

Modelling myopathic progression is based on the effects of the disease on the individual muscle fibres. Randomly, muscle fibres become diseased and begin to atrophy, while at the same time, still healthy muscle fibres hypertrophy slightly. As the disease progresses, more and more fibres become diseased. Exactly simulating this simple description of disease progression would involve the specific tracking of all the muscle fibres of a MU -- a computationally demanding, and likely unnecessary task. A more practical method of simulating myopathic progression is to steadily decrease the mean fibre diameter while increasing the standard deviation of diameters. Fibre diameters less than the specified lower bound of 25μm are set to zero, thus simulating the effect of fibre loss. In order to test the ability to track the advance of myopathy, simulations need to be done at several steps of the progression. Decreasing the mean diameter in steps of 3μm from 70μm to 46μm, while increasing the standard deviation of diameters from 6μm to 30μm in steps of 3μm, results in nine stages of myopathic progression being simulated.

*Results of SMUAP simulations*

In order to verify model implementation, the results demonstrated by McGill [29] are reproduced in figure 3.3 using the model parameters described above. He simulated SMUAPs from two depths and three electrode locations. Each of these six plots was repr ..ced well despite the changes made in several of the model parameters including fibre diameter, number of fibres per MU, tissue conductivity, and conduction velocity. The effect of these parameter variations is studied in more detail later. The most

noticeable difference between the present results and those by McGill is the order of magnitude difference in peak-to-peak amplitude of the action potentials, which is simply explained by the doubling of fibre diameter and the more than doubling of the number of fibres per MU. Amplitude, though, as will be discussed later, will not be used to characterize the SMUAPs. From the six simulations (fig. 3.3) it is clear that while the signal becomes weaker as the electrode is moved away from the endplate toward the tendon, measurement from between the endplate and the tendon provides a broader (temporally), and triphasic SMUAP. It may be then that the SMUAPs measured from the mid-point between the tendon and endplate provide more information about the state of the MU than do potentials measured from directly above the endplate. So it is with mid-point electrode placement that the SMUAPs are simulated.

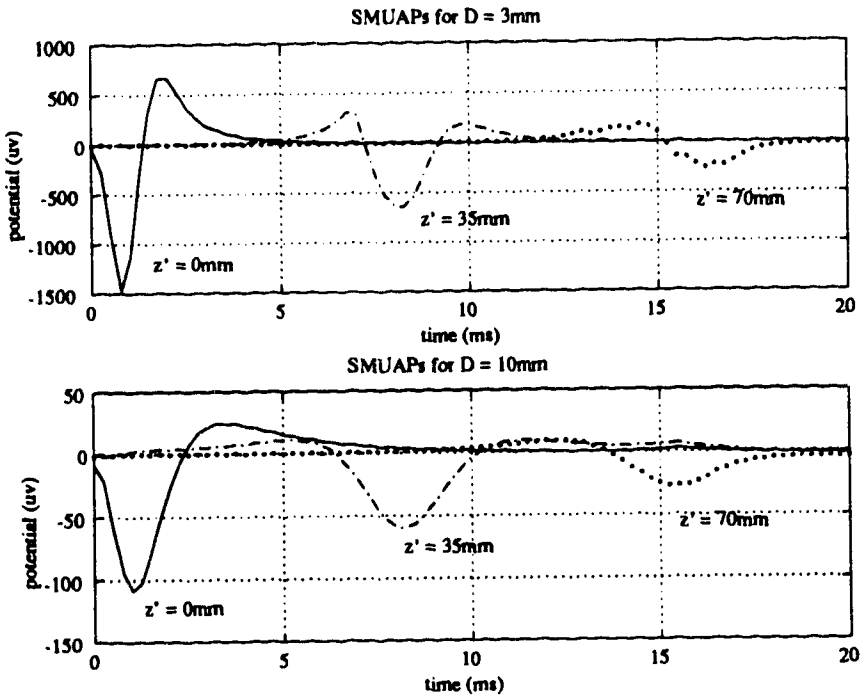


**Figure 3.3** Simulated SMUAPs. D is the transverse distance from the electrode to the center of the MU, and z' is the axial distance from the electrode to the center of the end plate zone.

*SEMG Modelling*

On the skin surface more than a single SMUAP is present: the SEMG is a spatial and temporal superposition of SMUAPs. Each MU contributing action potentials to the SEMG can be modelled as a black box with impulse response $\Phi_m(n)$, which is excited by a train of unit impulse functions $\Delta_m(n)$ (see fig. 3.4). This impulse train represents the firing signal from the motor neuron, and the impulse response represents the motor unit action potential.

$$\Delta_m(n) \longrightarrow \boxed{\Phi_m(n)} \longrightarrow \psi_m(n)$$

**Figure 3.4** Simulated SEMG block diagram. This is the SEMG due to a single motor unit.

The SEMG, $y(n)$, is comprised of the superposition of $\psi_m(n)$, and can then be described by the summation of the convolutions of each MU's impulse response and impulse train [12]:

$$y(n) = \sum_{m=1}^{M} \psi_m(n) \tag{3.6}$$

$$\psi_m(n) = \sum_{\eta=0}^{\infty} \Phi_m(\eta) \cdot \Delta_m(n-\eta), \tag{3.7}$$

where $M$ is the number of active MUs.

Determining the recruitment of motor units is important for determining the number of SMUAPs and consequently the amount of interference (between single MU signals) present in the SEMG. That is, the more SMUAPs there are overlapping in the SEMG, the more interference the SEMG is said to possess. The number of MUs recruited at a given point in time is dependent upon the level of contraction. It is not until about 75% of maximum voluntary contraction (MVC) that nearly all the MUs are firing [12]. Therefore, reducing the level of contraction will reduce interference, but will also reduce the scope of the data (i.e. reflecting information from fewer MUs). A major objective of analyzing the SEMG interference pattern is to take advantage of as broad a

physiologic scope of information as is possible Therefore, for these simulations, full recruitment is assumed.

The type of electrode and the electrode configuration used in measuring the SEMG also plays a very important role in the degree of interference present in the measured signal. The above SMUAP model, where the measurement is made at a point, corresponds to a measurement made with a very small monopolar electrode. Increasing the size of the electrode will result in spatial integration of SMUAPs, which is undesirable because it does not increase interference per se, but does increase blurring. Therefore, all signals in the following simulations are assumed to be from point electrode measurements. While this assumption is ideal and not truly practical, very small pin-like surface electrodes that penetrate only the top few layers of skin have been used successfully [15,16]. Such electrodes minimize the effect of electrode spatial integration, and remove the deleterious effects of the high resistance outer layer of skin.

Manipulating the degree of interference present in the SEMG signal can be done by varying the electrode configuration. A monopolar or a wide bipolar ('wide' referring to inter-electrode spacing distances of ~20mm) configuration results in high levels of interference. Differentiating electrode configurations will narrow and accentuate the nearer, stronger SMUAPs while suppressing the others, yielding much less interference. Presumably, all SEMG decomposition techniques will become more effective as the level of interference is reduced, while greater amounts of interference should possess information from a greater number of MUs. In an attempt to examine bicepstral deconvolution as a robust tool for analyzing SEMGs, monopolar electrode configurations are simulated.

In order to model the interference of SMUAPs, the spatial distribution of MUs must be determined. Using knowledge of the muscle fibre diameter, the number of fibres per motor unit, and various geometric measures of the muscle being considered, the interference signal is simulated. If MUs are identified by their center point, and assuming that the muscle fibres account for 100% the cross sectional area of the muscle, then the density of MU centers is

$$\rho = \frac{1}{N \cdot a^2}. \tag{3.8}$$

In the case of the brachial biceps, using $N = 225$ and $a = 70\mu m$, one finds a density of 0.907 MUs per square mm. Obviously, 100% of the muscle cross section is not fibres, but this assumption greatly simplifies the modelling of muscle and is balanced by slightly biased estimates of fibre size and number of fibres per MU, as previously mentioned. Then, if full MU recruitment is assumed, an estimate for the number of motor units at varying depths is calculated.

The most accurate model distributes the MU centers continuously with respect to radial distance and angle from the electrode. But, because each SMUAP to be used in the simulated SEMG is computed numerically, it is more efficient to pre-calculate a data bank of SMUAPs at discrete locations. Drawing simulated SMUAPs from this data bank, SEMGs can be simulated quickly. With reference to the geometric description of the muscle cross section seen below (fig. 3.5), the distribution of MU centers is compiled. Consider there to be a depth, S, of tissue separating the muscle fibres from the surface electrode, and that no MU centers exist less than a distance R from the top of the region of muscle fibres. R then is the radius of distribution of muscles fibres in a given MU, which, for the brachial biceps, is 2.5mm. If a step size of 1mm is used, and S, the connective tissue thickness, is set to 2mm, then SMUAPs must be simulated for MU center distances from 5mm to the point where th are insignificant. There is a factor of 10 difference in amplitude between signals from [illegible] n and 13mm; thus indicating that 9 discrete radial steps of 1mm should be used.

In order to minimize the number of unique locations for which SMUAP simulations must be compiled, the tissue is considered isotropic with respect to bioelectric signal propagation, and the angular axis is ignored. Then, all the SMUAP simulations for a given absolute MU center to electrode distance are done by placing the MU center directly below the electrode (in the x-y plane). The assumption that muscle is isotropic is not valid in general, but it is reasonable for this model. Schmidt and Pilkington found that, for skeletal muscle, modelling conductivity anisotropy can be done quite accurately by means of boundary extension [39]. This means that if the conductivity of muscle tissue is different in radial and transverse directions, then this difference can be accounted for in a model by changing the ratio of the fiber depth to fiber length. Further changing of the fiber depth can be used to account for the difference in conductivity between muscle, fat and skin. However, this brings about the fact that fibre depth and

length may change tremendously form one patient to the next. In fact, within a given patient, the change in fibre length due to contraction has a significant effect on the fibre's conduction velocity and, therefore, its SFAP as well [35]. Once again then, the issue of arbitrary modelling simplifications comes up, and once again, the objectives of this modelling dictates that no purpose is served by including such complications as tissue anisotropy and fibre length variation in this model at this point. The conductivity of soft tissue is thus considered to be isotropic and roughly constant throughout the body, ignoring the high resistance outer layer of skin.

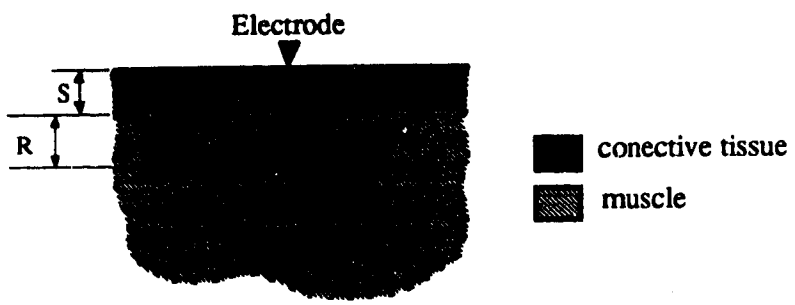


**Figure 3.5** A cross section of muscle. Shows region containing MU centers and the radial divisions used to quantize subregions.

A region of muscle bound by $r_i$ and $r_{i+1}$, as indicated in figure 3.5, is defined by the mean distance from electrode to MU center, $D$, which quite clearly is defined by $D = \frac{r_i + r_{i+1}}{2}$. The area of such a region can be determined through simple geometry. First, the area of the segment of the circle bounded by the arc of radial distance $r$ and the cord defining the closest possible MU center is equal to [40]

$$A_{seg}(r) = \frac{\pi r^2}{2} - \left[ D_0 \sqrt{r^2 - D_0^2} + r^2 \sin^{-1}\left(\frac{D_0}{r}\right) \right], \tag{3.9}$$

where $D_0 = S + R$.

Then the incremental area of MU centers at a mean distance $D$ is this segment area for $r = r_{i+1}$ minus the segment area for $r = r_i$.

$$A_{inc}(D) = A_{seg}(r_{i+1}) - A_{seg}(r_i) \tag{3.10}$$

Then, with 0.907 motor units per mm$^2$, the number of MUs for mean distances from 5 to

13 mm is tabulated below. For S = 2mm and R = 2.5mm, table 3.2 shows the distribution of MU center for $5mm \leq D < 13mm$.

| range $r_1$ - $r_2$ (mm) | mean distance D (mm) | Incremental Area ($mm^2$) | Number of MUs (rounded) |
|---|---|---|---|
| 4.5 - 5.5 | 5 | 4.30 | 4 |
| 5.5 - 6.5 | 6 | 8.65 | 8 |
| 6.5 - 7.5 | 7 | 12.21 | 11 |
| 7.5 - 8.5 | 8 | 15.57 | 14 |
| 8.5 - 9.5 | 9 | 18.85 | 17 |
| 9.5 - 10.5 | 10 | 22.08 | 20 |
| 10.5 - 11.5 | 11 | 25.28 | 23 |
| 11.5 - 12.5 | 12 | 28.48 | 26 |
| 12.5 - 13.5 | 13 | 31.65 | 29 |
| Totals | -- | -- | 152 |

**Table 3.2** The distribution of MU centers. Using equations (3.9) and (3.10) the area of isoradial region is calculated and shown in the third column. Then using ρ from equation (3.8), the number of motor unit centers is determined and tabulated in the fourth column.

Therefore, each SEMG simulation is comprised of 4 SMUAPs generated from a distance of 5mm, 8 from a depth of 6mm, 11 from 7mm, and so on.

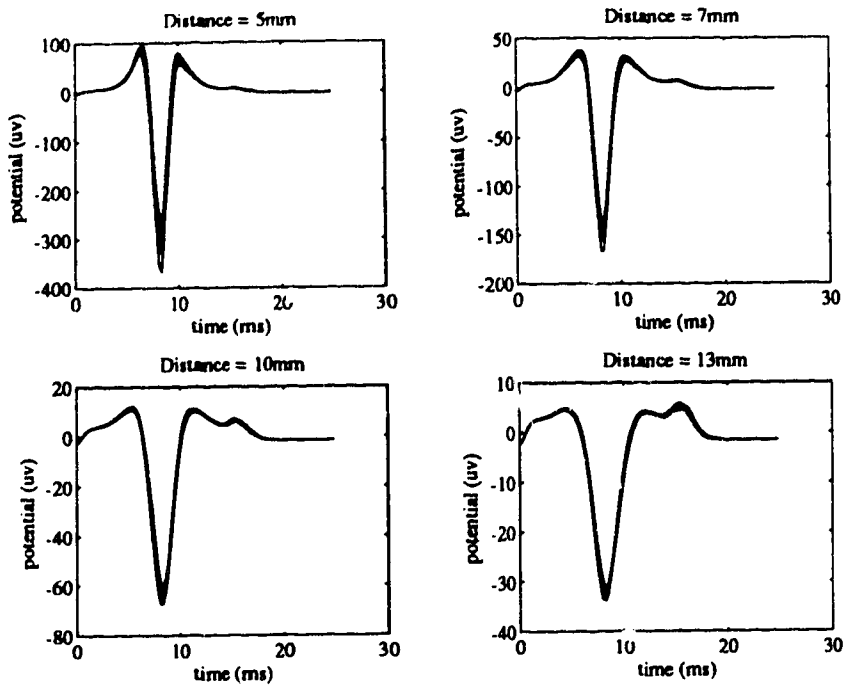


**Figure 3.6** Stage 1 simulated SMUAPs -- 20 per graph.

The data bank must provide an adequate number of SMUAP simulations to choose from for every given electrode-MU center distance and pathophysiologic state to account for random variability of muscle fibre distribution within a given MU. As can be seen (fig. 3.6), almost no variance exists in simulated SMUAPs at stage 1, even from very shallow depths. At stage 5 (fig. 3.7), variance between simulations becomes slightly more obvious, particularly at 5mm distance, then by stage 9 (fig. 3.8), the variance between simulations is quite significant at both the 5 and 7mm distances. In order to ensure that SEMG simuations are truly random, the size of each data bank is set to 100 simulations per distance, resulting in 900 SMUAPs to choose from for every disease stage.

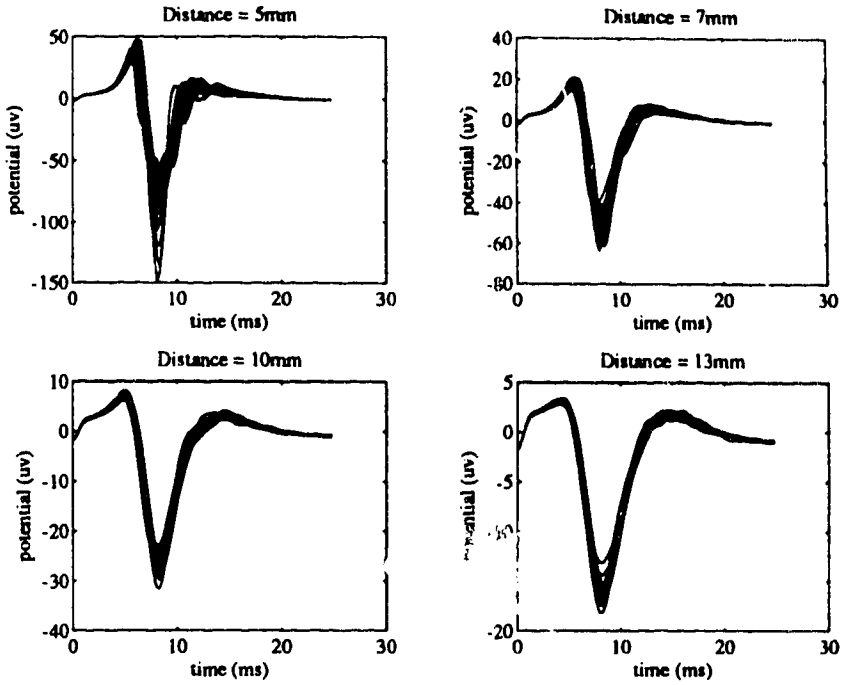


**Figure 3.7** Stage 5 simulated SMUAPs -- 20 per graph.

Finally, in order to properly combine the SMUAPs from the data bank to simulate a SEMG, the temporal distribution (i.e., firing rates) of SMUAPs needs to be considered. Firing rates vary through a range of roughly 5Hz to 25Hz, and are dependent upon the level of contraction and the particular MU in question. As the level of contraction increases, the firing rate of previously recruited MUs may increase as new MUs are recruited. At any one time there will be a relatively wide range of firing rates present, and because these varying rates apply to uniquely shaped MUAPs, the SEMG is modelled with a distribution of firing rates, not just the mean rate. At full recruitment, all MUs are firing at their maximal rate; these rates range primarily between 10 and 25Hz [12], and are distributed roughly normally [41]. A reasonable distribution for the firing rates should then be Gaussian with a mean of 17Hz and a standard deviation of 3Hz. Ideally, each of the 152 contributing MUs would be assigned a mean firing rate from a wide normal distribution, and each firing rate would vary within a small normal distribution. However, due to the high levels of superposition in the SEMG, and the similarity in shape of all SMUAPs, the inter-pulse interval for every MU is drawn from the same distribution. This simplification would cause problems only if particular

SMUAPs were being extracted from the SEMG, because they would not possess unique firing rates. Further investigation to the importance of firing sequences of SMUAPs occurs in chapters 4 and 5.

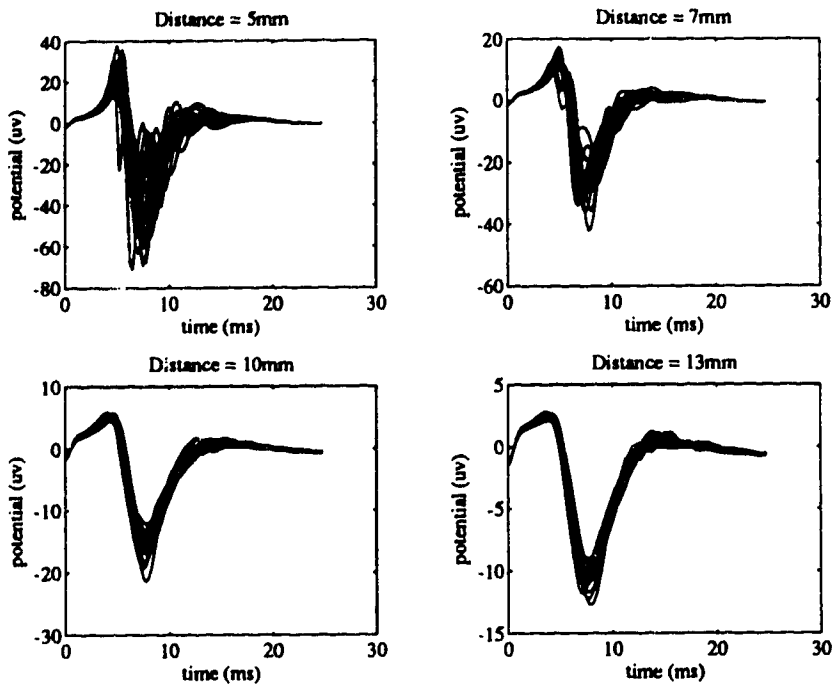


**Figure 3.8** Stage 9 simulated SMUAPs -- 20 per graph.

Implementing the combination of SMUAPs for SEMG simulation is done by first randomly extracting, from the data bank, the appropriate number of SMUAPs for each radial distance. For each SMUAP a sequence of interpulse intervals is selected randomly from a normal distribution with a mean of 60ms and a standard deviation of 8ms. Each sequence is then cumulatively summed to form a sequence of placement times for a given SMUAP. In order to avoid synchronization, each sequence is then offset by a random value chosen from a uniform distribution between 0 and 60ms. Mathematically, the simulation can be summarized as

$$y(n) = \sum_{j=D_{min}}^{D_{max}} \sum_{m=1}^{M_j} \sum_{i} \Phi_{j,k(m)}(n-\tau_i). \tag{3.11}$$

This represents a sum over electrode-MU center distances $j = D_{min}$ through $j = D_{max}$ of

all the SMUAPs $\phi(n)$. At each distance $j$ there are $M_j$ contributing MUs, $k(m)$ is a random variable uniformly distributed between 1 and 100, denoting a random choice of the $m$th SMUAP from the data bank, and $\tau_i$ is the cumulative sum of the Gaussian distributed impulse intervals of motor neuron unit impulse train $\Delta_m(n)$ after $i$ impulses. A pictorial representation of the synthesis model is shown in figure 3.9. While this model is effective for simulating SEMGs it represents, mathematically, a non-invertible equation. That is, there is no way to determine $\Phi_m(n)$ for all $m$ given only $y(n)$. Therefore, the following section develops a model of the SEMG for the purpose of analysis.

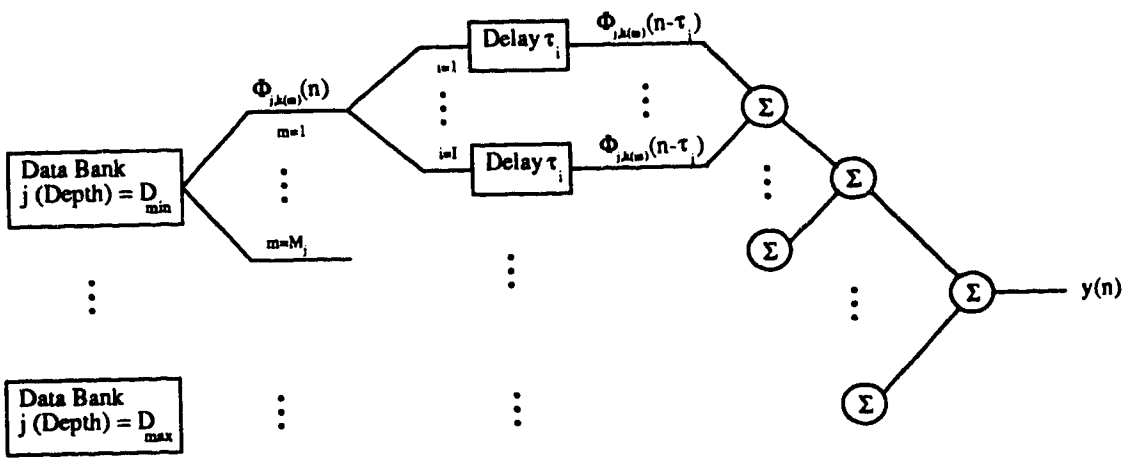


**Figure 3.9** A pictorial description of the synthesis model. The three levels of summing correspond, from left to right, to: the convolution of the SMUAP with the motor neuron impulse train, summing all contributions from a given isoradial region, and summing the net contribution from all isoradial regions.

*The Analysis Model*

This section develops the analysis model of the SEMG, which is used to justify and modify the bicepstral deconvolution algorithm as a method of analyzing the SEMG. Deconvolution, in the context of the discussion of chapter 2, is a procedure applied to the output of a LTI system with the objective of determining either the system's input and/or the system's impulse response. Therefore, the first step in creating an analysis model is to fit the synthesis model to a single-input, single-output, LTI system. The SEMG

clearly has only one output, but according to the synthesis model, it has many inputs, and many impulse responses. Each contributing MU has an independent sequence of motor neuron impulses triggering it (ignoring the phenomenon of motor neuron firing synchronization due to fatigue), and each resulting MUAP is determined only by the geometry and pathophysiologic states of its particular MU's muscle fibers.

Equation (3.11) from the synthesis model can be rewritten, not to represent how the SEMG simulation is implemented, but rather to represent the process taking place in the simulation. Instead of considering the SEMG as a triple summation of SMUAPs, it may be described as the sum of all the signals generated by every contributing MU. Each of these signals results from the convolution of the train of unit impulse functions from the motor neuron, with that SMUAP:

$$y(n) = \sum_{m=1}^{M} \Phi_m(n) * \Delta_m(n), \tag{3.12}$$

where both the impulse train and the SMUAP are unique for every MU. Describing the SEMG in terms of convolution, as done above, is the first step towards creating a model that can be inverted using bicepstral deconvolution. However, (3.12) still contains $M$ inputs and $M$ system impulse responses.

The next step in remodelling the SEMG is to reduce it to having a single input. It has already been justified, as part of the synthesis modelling, that each motor neuron unit impulse train can be assumed to have identical characteristics, so it is reasonable to define a single input to the system, $\upsilon(n)$, as the sum of all the unit impulse trains.

$$\upsilon(n) = \sum_{m=1}^{M} \Delta_m(n) \tag{3.13}$$

Following this, the logical step is to define a single system impulse response, which is representative of the SMUAPs from the entire volume of muscle contributing to a SEMG. This system impulse response is heretofore referred to as a representative surface-measured motor unit action potential (RSMUAP).

The difficulty in the RSMUAP definition arises from the fact that each SMUAP is considered unique by the synthesis model. For a given electrode-MU center distance this uniqueness can be simplified by assuming that all the SMUAPs are identical, and

equal to the time domain average of all the contributing SMUAPs from that given distance. From this point, recalling that the tissue is modelled as purely resistive, it is reasonable to say that the primary difference between SMUAPs of different distances is their amplitudes. So then, it is also reasonable to say that a single system impulse response of unit amplitude may be able to represent all the normalized SMUAPs contributing to a given SEMG.

As shown in figure 3.10, the assumption that all normalized SMUAPs are identical is not true. The shallow MUs contribute much less signal from the distal portions of their muscle fibers, while the distance from the electrode to one point on a deep fiber or another is not much different, thus, the contribution by lengthwise regions of the muscle fibers is more equal. This has a noticeable effect on the SMUAP shape, which is highlighted by the late potential resulting from poles remaining stationary at the tendons. This phenomena is discussed in more detail by Stegman et al. [42]. However, the result of a time domain average of all the contributing SMUAPs is quite consistent for a given disease stage, where the contributing SMUAPs are choosen randomly from the data bank in exactly the same manner that they are choosen for SEMG simulation. Figure 3.11 shows fifty such averages overlaid for stages 1, 5, and 9, and for each stage there is virtually no variance between trials. Thus, the RSMUAP of a given SEMG is the time-domain average of all contributing SMUAPs.

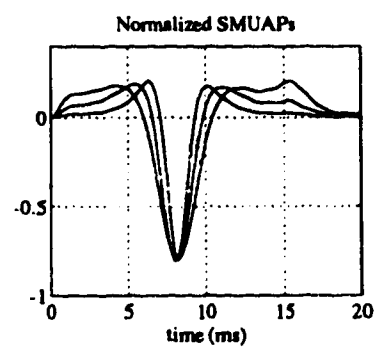


**Figure 3.10** A comparison of normalized SMUAPs. Shown are simulations from 5mm, 9mm, and 13mm.

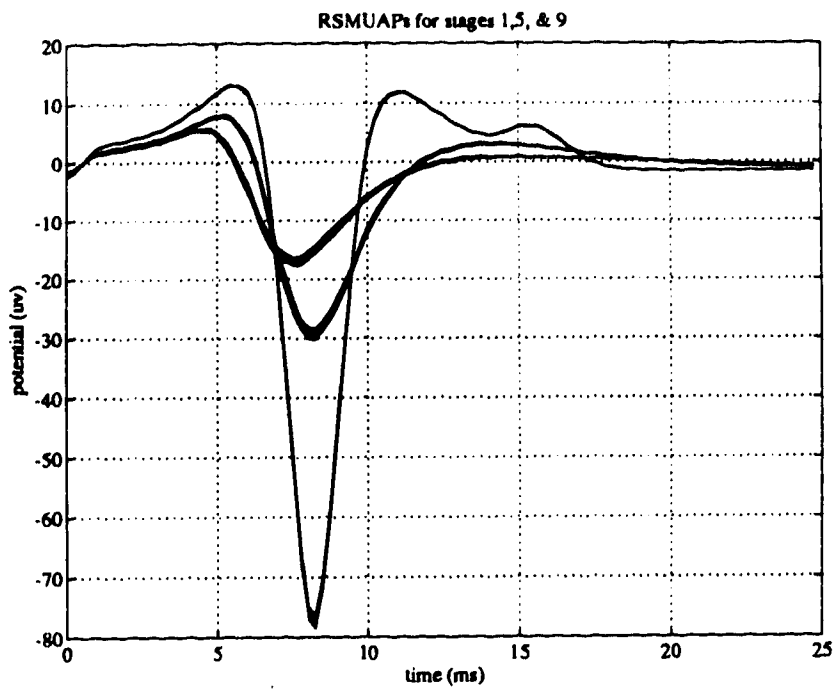


**Figure 3.11** Simulated RSMUAPs. Stage 1 being the largest (peak to peak) RSMUAP and stage 9 being the smallest.

If this definition of the RSMUAP is to be used as the sole response of a LTI system, it follows that it must have a fixed amplitude. This definition, however, creates a conflict with the convolution equation (3.12) above, which dictates that the system input is comprised only of unit amplitude impulses. As well, in reality, the motor neuron impulses, trigger the all-or-none muscle fiber action potential, which has an amplitude that is entirely independent of the triggering impulse. However, this can be rationalized by modifying the definition of the system input, $\upsilon(n)$, to allow it to modulate the RSMUAP amplitude according to MU depth. Therefore, by normalizing the RSMUAPs instead of the input impulses, each impulse possesses the amplitude of the SMUAP it is intended to generate. This amplitude modulating system input is referred to in this thesis as the firing sequence. The SEMG, $y(n)$, is thus modelled for analysis as the convolution of the firing sequence with the unit amplitude RSMUAP. That is,

$$y(n) = \upsilon(n) * \zeta(n), \tag{3.14}$$

where

$$\upsilon(n) = \sum_{m=1}^{M} \hat{\Phi}_m \cdot \Delta_m(n), \tag{3.15}$$

and

$$\zeta(n) = \frac{\xi(n)}{\hat{\xi}}; \tag{3.16}$$

given that

$$\xi(n) = \sum_{m=1}^{M} \Phi_m(n), \tag{3.17}$$

and $\hat{\Phi}_m$ and $\hat{\xi}$ are, respectively, the peak to peak amplitudes of $\Phi_m$ and $\xi$ .

*Signal Requirements*

With a model schematically matching the system depicted in figure 2.1, the characteristics of the system's input and impulse response should be examined before the bicepstrum is applied for deconvolution of the SEMG. A requirement for the validity of equation (2.61), which is an essential basis in the derivation of the bicepstral deconvolution algorithm, is that the input to the LTI system is a non-Gaussian, white, stationary random sequence. Most certainly, the most important of these restrictions is that the input sequence be non-Gaussian, because, as pointed out in chapter 2, the 3rd order cumulant sequence of a Gaussian sequence is strictly zero. If the firing sequence is indeed non-Gaussian and white, the bispectrum of the SEMG, with the exception of a constant magnitude factor, is simply the bispectrum of the RSMUAP (see eq. (2.58)). Make note that, by the same logic, the system impulse response must be non-Gaussian, but that is evident from the RSMUAP plots in figure 3.10.

The synthesis model can be modified to generate firing sequences corresponding to the SEMGs it simulates. A train of impulses is generated by inserting an impulse at each point in time that a SMUAP is inserted from the data bank into the SEMG. Making the amplitude of each of these impulses equal to the peak-to-peak amplitude of the SMUAP which it is intended to be triggering, produces a simulated firing sequence. With 152 impulse trains contributing to the firing sequence, a mean interpulse interval of

60ms, and a sampling period of 1ms, there is an extensive overlap of impulses. This overlap makes the firing sequence look like a random sequence, rather than a train of impulses. This random sequence should have a probability density function (p.d.f.) skewed toward the smaller values due to there being more MUs at greater distances than at nearer distances. That is, there are more relatively low amplitude SMUAPs contributing to the SEMG than there are high amplitude ones. This means that it is expected that the p.d.f. of the firing sequence should have a finite and significant 3rd order moment, which, by definition, means that it is non-Gaussian. A segment of a simulated firing sequence, its spectrum and p.d.f. are shown in figure 3.12 along with the p.d.f. of a similar Gaussian sequence for comparison. The Gaussian sequence is equal in mean and variance to the firing sequence, but the firing sequence has a slightly non-zero coefficient of skewness, while the Gaussian sequence has a near negligible skew. The coefficient of skewness, or more simply, the skew is defined as

$$skew = \frac{\mu_3}{(\mu_2)^{3/2}}, \tag{3.18}$$

where $\mu_2$ and $\mu_3$ are respectively the second and third order moments of $\upsilon(n)$:

$$\begin{aligned} \mu_2 &= E\left[\upsilon^2(n)\right] \\ \mu_3 &= E\left[\upsilon^3(n)\right] \end{aligned}. \tag{3.19}$$

Recall from chapter 2 that the third order cumulant sequence of a Gaussian process is zero, and therefore, so is its bispectrum. Figure 3.13 shows the magnitudes of the bispectra of the firing sequence and the Gaussian sequence, and demonstrates the necessity of the firing sequence having a non-zero skew.

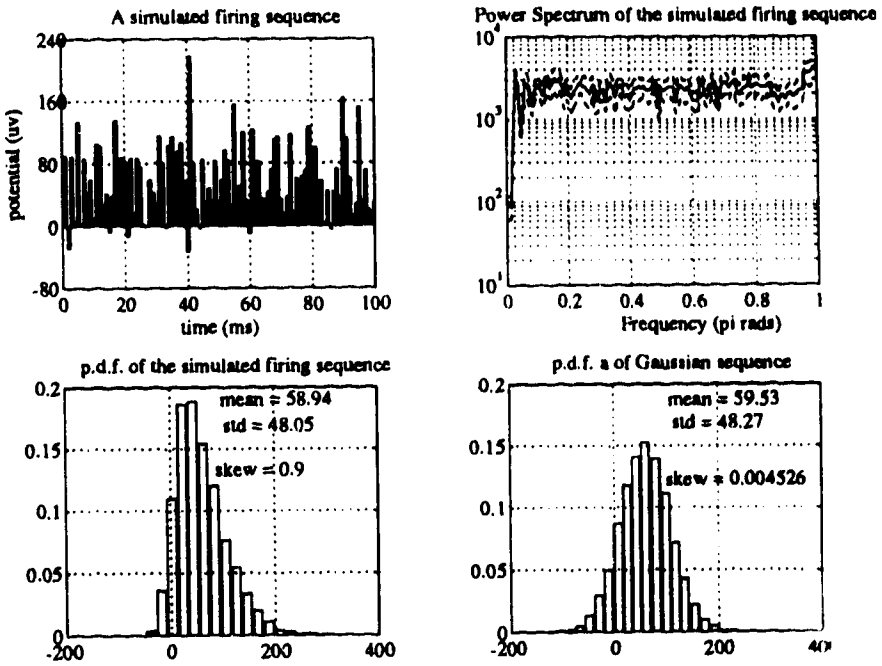


**Figure 3.12** The characteristics of the simulated firing signal compared with a Gaussian sequence.

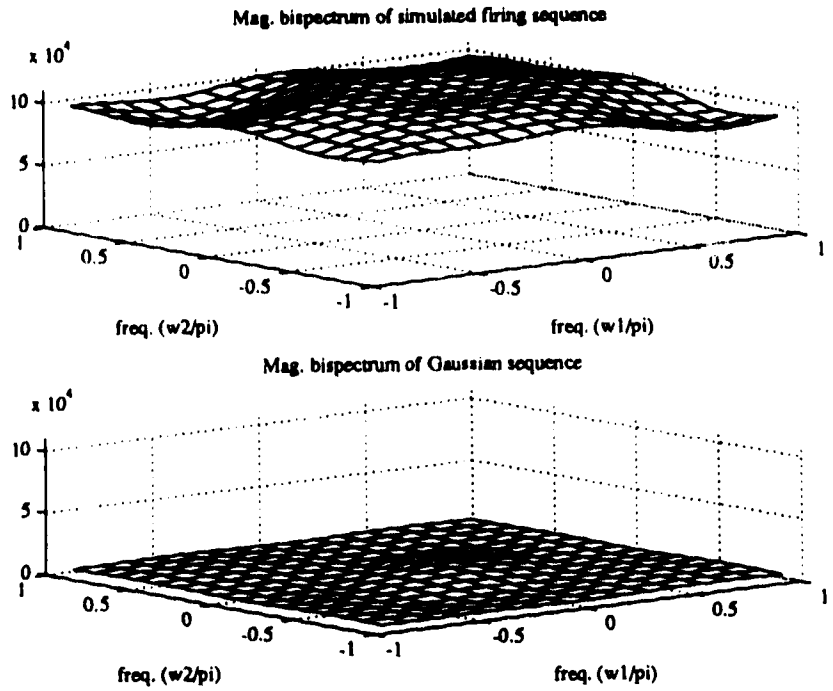


**Figure 3.13** The magnitude bispectra of skewed and non-skewed signals.

# Chapter 4
# Methods and Results

*Parameter Determination*

RSMUAPs are deconvolved from SEMGs using bicepstral deconvolution as described in chapter 2, where the SEMG is considered the output of a LTI system, and the RSMUAP is the system's impulse response. The quality of the RSMUAP estimated from bicepstral deconvolution depends upon the selection of the following algorithm parameters: ① sampling frequency of the data, ② the number of cepstral coefficients from which the RSMUAP is reconstructed, and ③ the amount of data. For now, the amount of data is considered unlimited, although the objective is to use a little as possible.

The sampling frequency of the SEMG, as one expects, is dependent upon its spectrum, which is shown for myopathic progression stages 1, 5 and 9 in figure 4.1. Clearly, all three spectra become effectively zero around 500 to 600 Hz, and therefore, with the 4000Hz sampling rate used in the simulation, the SEMG is well oversampled. The first and most important problem with deconvolving an oversampled signal is that cepstra are not defined for band-limited systems. By definition, a cepstrum involves the logarithm of spectrum, which is not defined if the spectrum is zero at any frequency. For the case of complex cepstra the power spectrum must be entirely non-zero. In the case of calculating the bicepstrum, the logarithm operation is applied to the magnitude of the bispectrum. If the magnitude of the bispectrum contains zeros, the logarithm operation becomes unstable and, consequently, the resulting impulse response estimates are unreliable. From the relation (2.40) between the bispectrum and the power spectrum, it is clear that the magnitude of the bispectrum is non-zero for all frequencies if and only if the same is true about the power spectrum. For that reason, only the power spectrum need be shown to be full band for the bicepstrum to be defined.

Because the power spectra of the simulated SEMGs show the signal to be band-limited only on the high freque .cy side (fig. 4.1), creating a full band signal can be achieved by resampling the SEMG with a sampling rate of 1000Hz. In order to avoid aliasing the SEMG is first filtered by an eighth order Chebyshev filter with a cut-off frequency equal to 500Hz (the Nyquist frequency of the resampling). The SEMG is filtered in both directions producing a sixteenth order magnitude roll-off, and zero phase distortion. Quite clearly, phase distortion at this stage of filtering would defeat the purpose of using higher order spectra to preserve the phase of the RSMUAP.

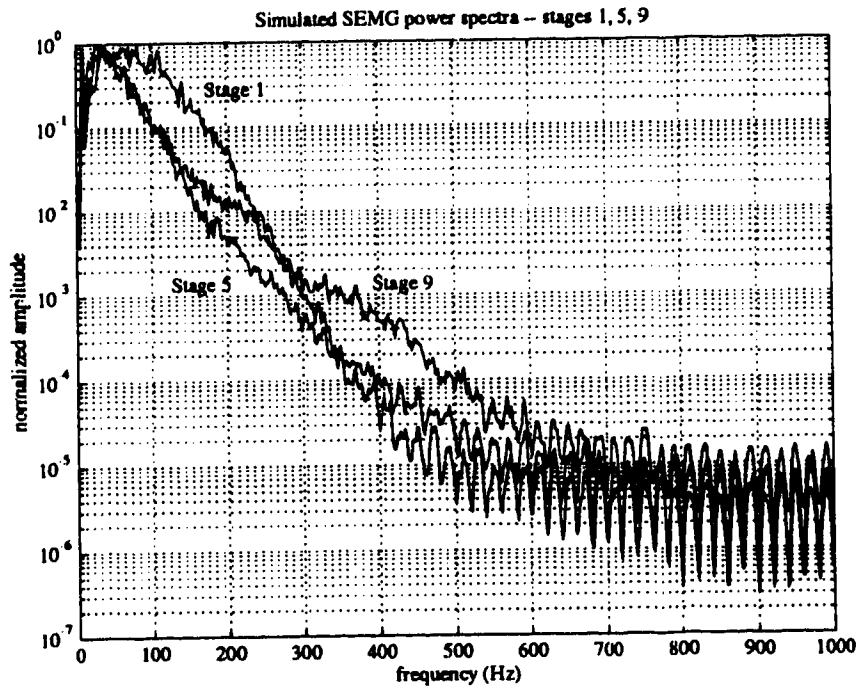


**Figure 4.1** Power spectra of simulated SEMG. Shown for myopathy stages 1, 5 and 9.

Another important reason for down-sampling the SEMG before deconvolution is to minimize computation time. The bicepstal deconvolution procedure is computationally demanding and must be repeated for every RSMUAP estimation. As the number of desired cepstral coefficients increases so does the size of the third order cumulant sequence, and therefore, so does every signal segment and in turn the overall length of the simulated SEMG. If, as is the case in this study, many simulations are desired for

statistical analysis, the total computation time becomes greatly increased by requiring more cepstral coefficients to be calculated. So, from a time perspective, the fewer samples the better.

With a sampling rate fixed, the minimum number of cepstral components can be determined. As discussed in chapter 2, estimating the number of significant cepstral components, $p$ and $q$, can be done directly from the third order cum[illegible]quences of the SEMG. Equation (2.60) shows that $A^{(k)}$ and $B^{(k)}$ of the cepstra[illegible]on are found directly in the 3rd order cumulant sequence. Therefore, inspecting the cumulant sequence should indicate the number of significant $A^{(k)}$ and $B^{(k)}$ terms.

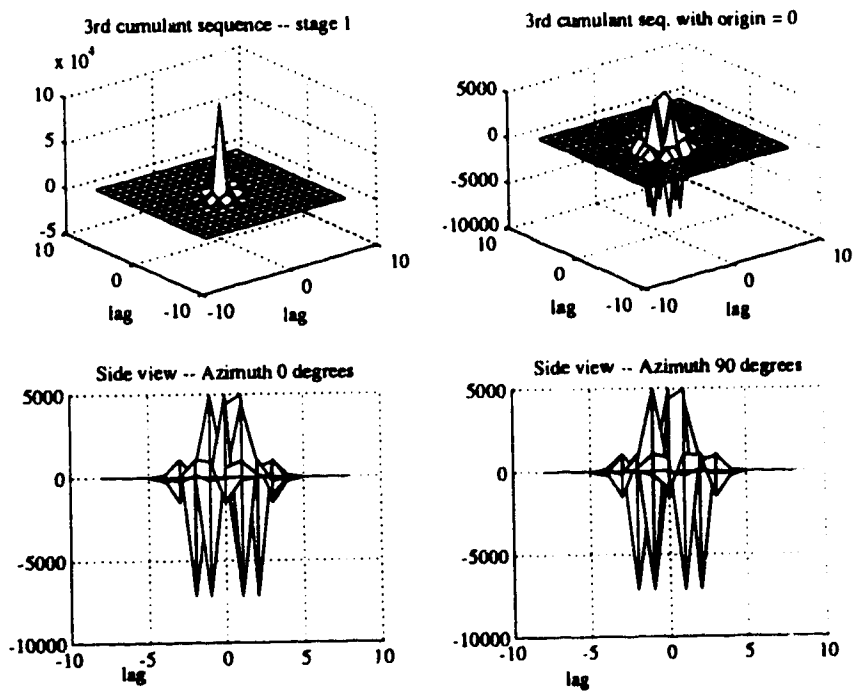


**Figure 4.2** Stage 1 third order cumulants of a simulated SEMG -- shown unaltered in the first frame, and following that with its origin set to 0.

Figure 4.2 shows that the dominant element of the 3rd order cumulant sequence of a stage 1 SEMG is at the origin. However, equation (2.60) shows that the origin of the 3rd order cumulant sequence does not contribute to the solution of the deconvolution. Therefore, to improve resolution of the meaningful elements, the origins of 3rd order cumulant sequences are set to zero. Following this, it is clear that there are no more than

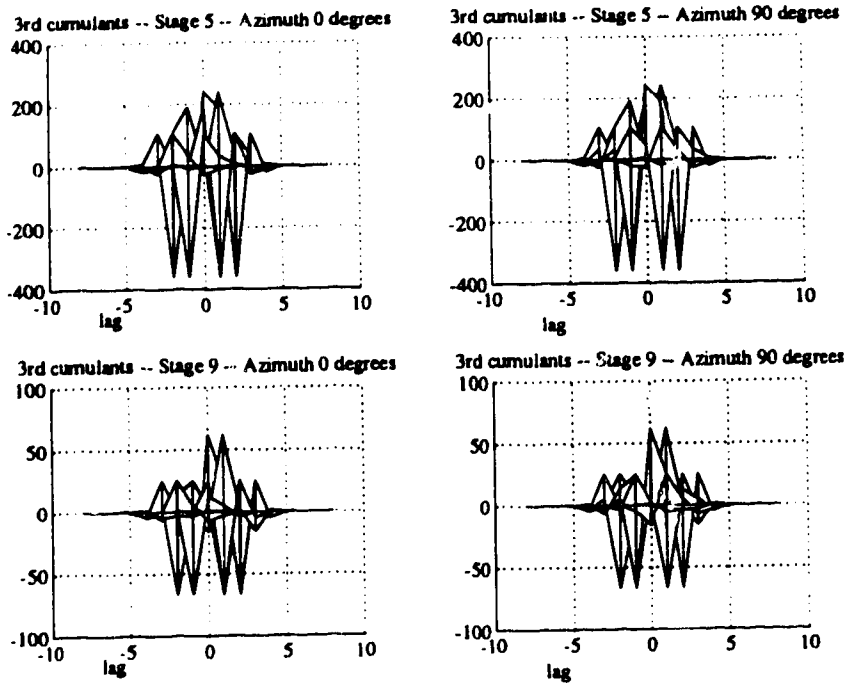


**Figure 4.3** Stages 5 and 9 third order cumulants of simulated SEMGs -- shown from the side, with origins set to 0.

four significant elements in the SEMG's cumulant sequence in any direction from the origin. Third order cumulant sequences of SEMGs from stages 5 and 9 (fig. 4.3) are noticeably different in shape, but again have no more than four significant elements in any direction. Thus, for all SEMG analysis, the cepstral equation may be truncated for both $A^{(k)}$ and $B^{(k)}$ at $k = p = q = 4$.

Determining the amount of data required empirically, it is found that ten seconds of simulated SEMG data is suitable for all the experiments in this thesis. Data length is discussed more in chapter 5.

### *The Algorithm*

Bicepstral deconvolution is performed using the MATLAB™ routine *biceps*, which is part of the Hi-Spec™ software package from United Signals & Systems, Inc.. The algorithm follows directly from its development in chapter 2, except the ten second SEMG, consisting of 10000 samples, is segmented into records of 256 samples each.

Overlapping these records by 50% results in a total of 77 records, and for each of these records, an estimate of the third order cumulant sequence is made using (2.36). It should be noted that (2.36) is a biased estimator of third order cumulants, which is used because Pan and Nikias found no improvement in bicepstral deconvolution by using an unbiased estimator [26]. The results of these cumulant sequence estimates are then averaged to produce an estimate of the third order cumulant sequence of the SEMG. The cepstal equation (2.63) is then solved using least squares, and the RSMUAP is estimated using (2.68), (2.69), and (2.70).

*Experiments*

Through the following section, the experiments are numbered with symbols ❶ through ❾, which are used to reference these experiments in the following chapter. For each of the nine stages of myopathic progression, 50 SEMGs are simulated, and from each of these SEMGs, a RSMUAP is estimated via bicepstral deconvolution ❶. Then, random, zero-mean, white Gaussian noise is added to these 50 SEMGs, and RSMUAPs are estimated from each ❷. Defining the noise as $w(n)$, the noisy SEMG is

$$y_n(n) = y(n) + w(n). \tag{4.1}$$

Characterizing the p.d.f. of the noise by its variance, $\sigma_w$, the signal to noise ratio (SNR) is defined as

$$\mathrm{SNR} \equiv 10 \cdot \log\left[\frac{\sum_n y^2(n)}{N\sigma_w^2}\right], \tag{4.2}$$

where $N$ is the total number of samples in $y(n)$. For each of the simulations, the variance of the noise p.d.f. is set such that the SNR equals 10dB, which corresponds to an average power ratio of 10:1.

The RSMUAPs resultant from experiments ❶ and ❷ are processed in two ways. First, the estimated RSMUAPs are compared with their ideal counterparts, the ideal RSMUAP being those simulated directly from SMUAPs as in figure 3.11, while the estimated RSMUAPs result from bicepstral deconvolution of the SEMG. In order to compare the shapes of the estimated and ideal RSMUAPs, their peak to peak amplitudes

are normalized to equal 1, their means are removed, and they are temporally aligned such that the large negative peak of each occurs at the same point in time.

Also, estimated RSMUAPs of differents stages of myopathic progression are compared with each other. Considering each time-domain sample of the RSMUAPs to be a different variable, each RSMUAP becomes a point in a hyperspace, and the collection of points from a given disease stage define a group. The dimension of this hyperspace is reduced using principal component analysis [43], then discriminant analysis is used to classify each estimated RSMUAP. First, the RSMUAPs are split into two sets, an observation set and a training set, each containing 25 estimated RSMUAPs per disease stage. The observation is defined by matrix $\mathbf{x}$, where each column contains the samples of a single RSMUAP. Then, each member of the observation set is classified into a disease stage group using the maximum likelihood discriminant function [43]

$$L_i\{\mathbf{x}\} = (\mathbf{x} - \boldsymbol{\mu}_i)' \boldsymbol{\Sigma}_i^{-1} (\mathbf{x} - \boldsymbol{\mu}_i) + \log|\boldsymbol{\Sigma}_i|, \tag{4.3}$$

where $\boldsymbol{\mu}_i$ and $\boldsymbol{\Sigma}_i$ are, respectively, estimates of the mean vector and covariance matrix of the training set members of disease stage $i$. Following this classification, the training and observation sets are switched, and the classification procedure is repeated.

In order to more fully examine the effects of noise, RSMUAP estimates are made from noisy SEMGs with SNRs ranging from 20dB to 0dB. Furthermore, the restriction that the noise be white is removed by lowpass filtering all the noise signals, $w(n)$, at 300Hz with a 3rd order FIR filter. This not only changes $w(n)$ into coloured noise, but may introduce more skew into noise that ideally has none. From chapter 3 figures 3.6, 3.7, and 3.8, it is clear that the greatest amount of variance between SMUAP simulations occurs for stage 9 of the myopathic progression, and therefore, it is reasonable to presume that stage 9 RSMUAPs will have the greatest variance between estimations. For this reason, stage 9 SEMGs are used to test the noise. Twenty simulations of stage 9 SEMGs are generated, and from each, four noisy simulations are created with SNRs equal to 20dB, 10dB, 5dB, and 0dB. Then 20 RSUAPs are estimated for each of the four SNR levels ●.

The final two experiments are designed to investigate the effect of the model on bicepstral deconvolution. First, the physical description of the muscle is modified by using 163 fibres per MU and a mean fibre diameter of 55μm, which are the values used by

Nandedkar et al. in their previously mentioned models. With these modifications, the SEMG model is referred to as model B and the previous as model A. Using model B, a mini data bank is built, containing 20 simulations per depth and for disease stages 1, 5, and 9. Given the relation (3.8), the number of MU centers per $mm^2$ becomes 2.03 for model B, which is roughly twice the number used in model A. For simplicity sake then, model B is implimented by using the same SEMG simulation twice while drawing the SMUAPs from the model B data bank. For stages 1, 5, and 9, 10 noise-free SEMGs are simulated, and from each an RSMUAP is estimated ❹.

The second experiment involving the modelling is done by modifying the firing signal. One of the assumptions of the modelling in chapter 2 is that the input signal (i.e. the firing signal) to the system in figure (2.1) is stationary. However, studies indicate that the firing patterns of motor neurons are not stationary, but rather that there is a decrease in firing frequency over time during muscular contraction due to fatigue [12,19,44]. Simulating a decrease in firing frequency is done by linearly increasing the mean interp interval of each MU from 60ms to 84ms over a ten second period. The firing signal is simulated 10 times for stage 9, then for each of the disease stages 1, 5, and 9, 20 SEMGs are simulated with this firing frequency gradient and RSMUAPs are estimated from each ❺.

*Results*

In the first experiment, ❶, RSMUAPs are estimated from noise-free SEMG simulations for all nine stages of myopathic progression. Ten of these estimated RSMUAPs from stage 1 data are shown in figure 4.4 along with an ideal RSMUAP generated from stage 1 SMUAPs. Figures 4.5 and 4.6 show similar results for disease stages 5 and 9, respectively.

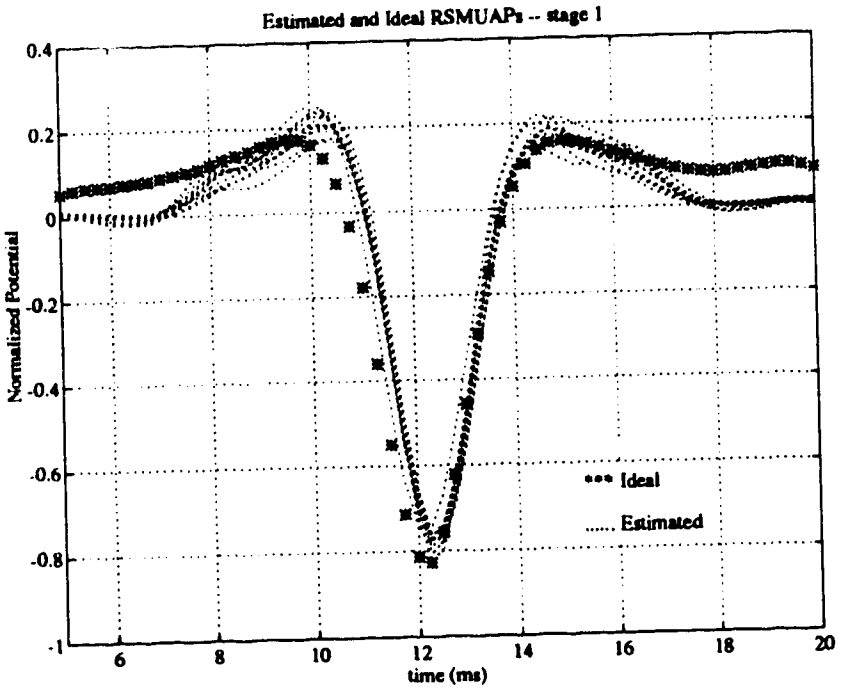


**Figure 4.4** Stage 1 RSMUAPs. Ten estimated RSMUAPs and one ideal RSMUAP from noise-free, stage 1 SEMGs.

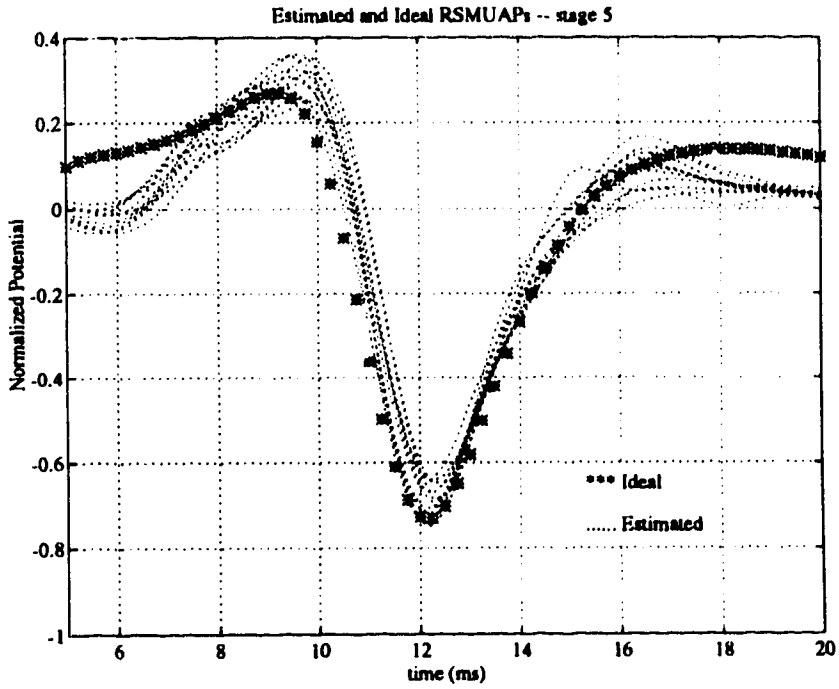


**Figure 4.5** Stage 5 RSMUAPs. Ten estimated RSMUAPs and one ideal RSMUAP from noise-free, stage 5 SEMGs.

The results of the discriminant analysis of the estimated RSMUAPs from experiment ❶ are shown in table 4.1, also known as a classification matrix. The results of this discriminant analysis are further tabulated (table 4.2) showing, by disease stage, the percentage of RSMUAPs correctly classified within one group of their correct classification.

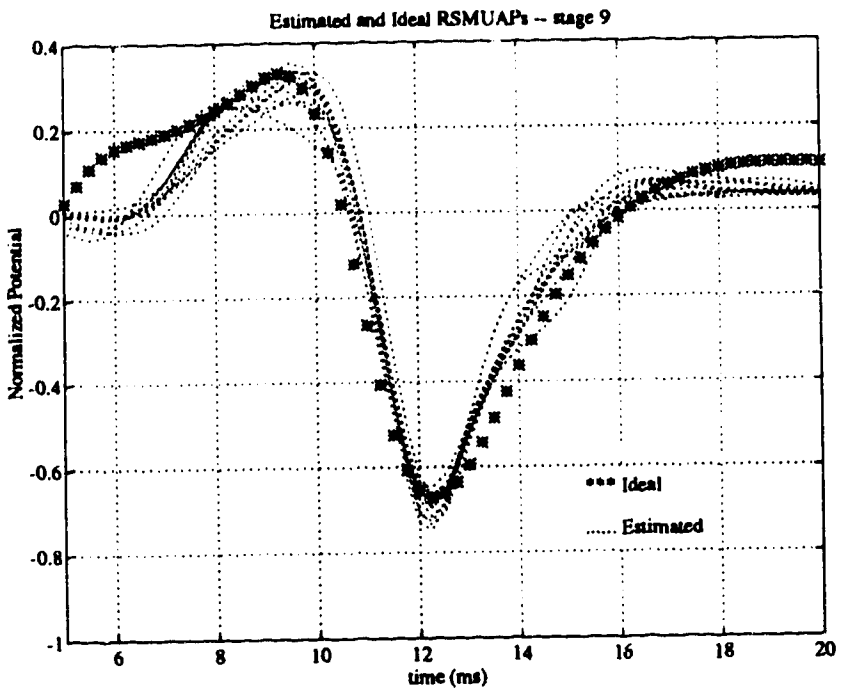


**Figure 4.6** Stage 9 RSMUAPs. Ten estimated RSMUAPs and one ideal RSMUAP from noise-free, stage 9 SEMGs.

| Stage # | 1 | 2 | 3 | 4 | 5 | 6 | 7 | 8 | 9 |
|---|---|---|---|---|---|---|---|---|---|
| 1 | 50 | 0 | 0 | 0 | 0 | 0 | 0 | 0 | 0 |
| 2 | 0 | 49 | 1 | 0 | 0 | 0 | 0 | 0 | 0 |
| 3 | 0 | 3 | 41 | 6 | 0 | 0 | 0 | 0 | 0 |
| 4 | 0 | 0 | 2 | 34 | 7 | 7 | 0 | 0 | 0 |
| 5 | 0 | 0 | 0 | 8 | 20 | 15 | 4 | 2 | 1 |
| 6 | 0 | 0 | 0 | 3 | 12 | 18 | 6 | 7 | 4 |
| 7 | 0 | 0 | 0 | 0 | 3 | 9 | 20 | 12 | 6 |
| 8 | 0 | 0 | 0 | 1 | 1 | 5 | 13 | 19 | 11 |
| 9 | 0 | 0 | 0 | 0 | 0 | 8 | 8 | 9 | 25 |

**Table 4.1** Classification matrix for noise-free RSMUAPs. Rows indicate true origin of RSMUAPs. Columns indicate into which group they are classified

| Group | 1 | 2 | 3 | 4 | 5 | 6 | 7 | 8 | 9 | mean |
|---|---|---|---|---|---|---|---|---|---|---|
| Percent correctly classified | 100 | 100 | 100 | 86 | 86 | 72 | 82 | 86 | 68 | 86.7 |

**Table 4.2** Classification accuracy for noise-free RSMUAPs. Percentage classified within one group of their correct classification

With the addition of Gaussian noise to the SEMGs used in experiment ❶, experiment ❷ generates similar results: figures 4.7, 4.8, and 4.9 show the comparisons between ideal and estimated RSMUAPs, and tables 4.3 and 4.4 are the results of the discriminant analysis.

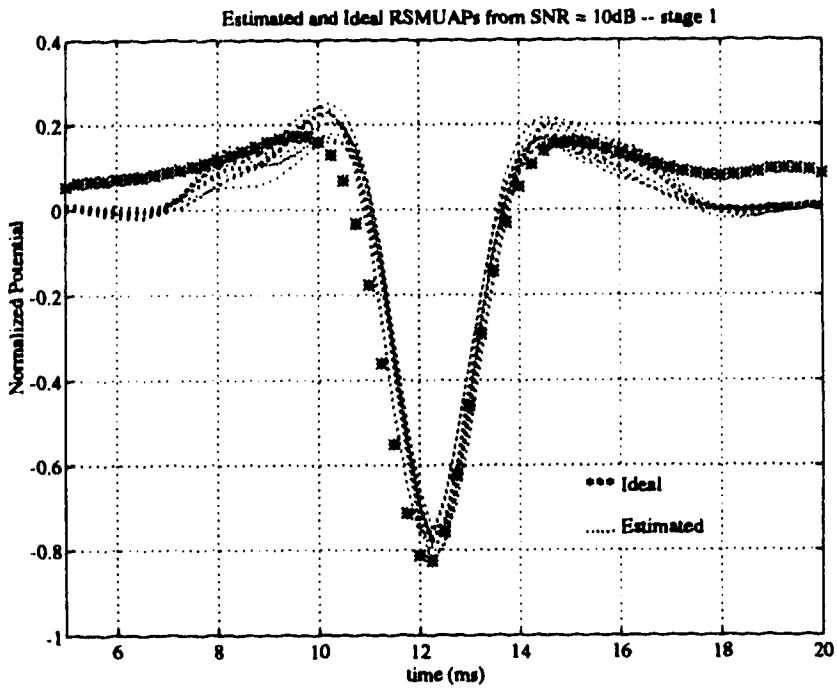


**Figure 4.7** Stage 1 Noisy RSMUAPs. Ten estimated RSMUAPs and one ideal RSMUAP from noisy, stage 1 SEMGs.

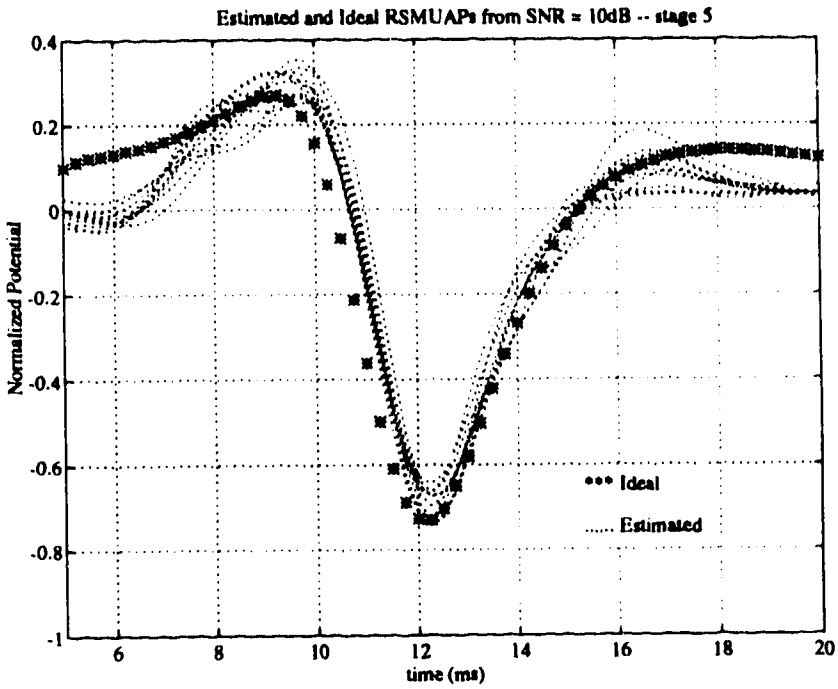


**Figure 4.8** Stage 5 Noisy RSMUAPs. Ten estimated RSMUAPs and one ideal RSMUAP from noisy, stage 5 SEMGs.

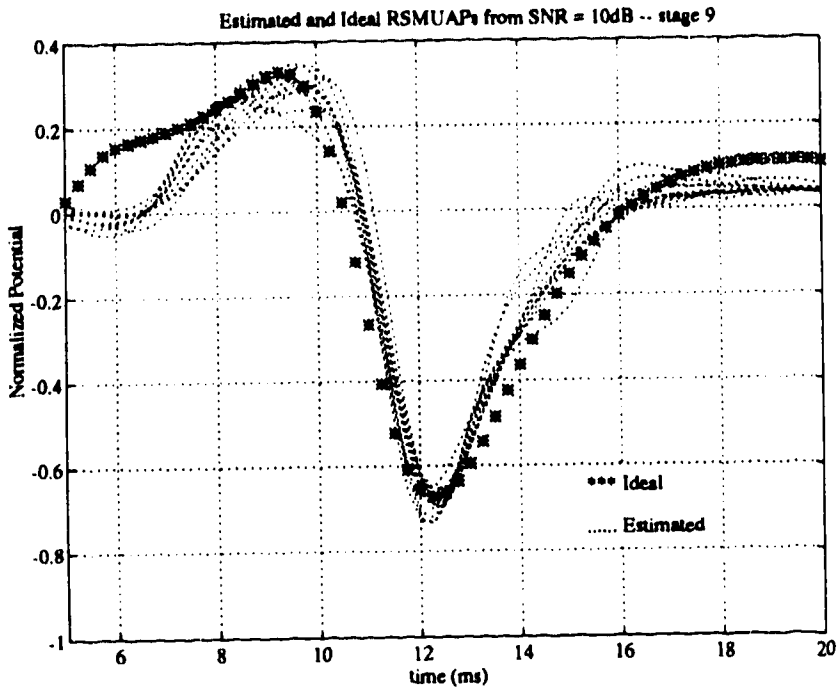


**Figure 4.9** Stage 9 Noisy RSMUAPs. Ten estimated RSMUAPs and one ideal RSMUAP from noisy, stage 9 SEMGs.

| Stage # | 1 | 2 | 3 | 4 | 5 | 6 | 7 | 8 | 9 |
|---|---|---|---|---|---|---|---|---|---|
| 1 | 50 | 0 | 0 | 0 | 0 | 0 | 0 | 0 | 0 |
| 2 | 0 | 48 | 2 | 0 | 0 | 0 | 0 | 0 | 0 |
| 3 | 0 | 2 | 43 | 5 | 0 | 0 | 0 | 0 | 0 |
| 4 | 0 | 0 | 5 | 24 | 12 | 5 | 3 | 1 | 0 |
| 5 | 0 | 0 | 0 | 5 | 23 | 16 | 4 | 1 | 1 |
| 6 | 0 | 0 | 0 | 1 | 16 | 19 | 6 | 6 | 2 |
| 7 | 0 | 0 | 0 | 0 | 4 | 6 | 15 | 17 | 8 |
| 8 | 0 | 0 | 0 | 2 | 2 | 7 | 9 | 16 | 14 |
| 9 | 0 | 0 | 0 | 1 | 0 | 6 | 7 | 15 | 21 |

**Table 4.3** Classification matrix for noisy RSMUAPs. Rows indicate true origin of RSMUAPs. Columns indicate into which group they are classified

| Group | 1 | 2 | 3 | 4 | 5 | 6 | 7 | 8 | 9 | mean |
|---|---|---|---|---|---|---|---|---|---|---|
| Percent correctly classified | 100 | 100 | 100 | 82 | 88 | 82 | 76 | 78 | 72 | 86.4 |

**Table 4.4** Classification accuracy for noisy RSMUAPs. Percentage classified within one group of their correct classification

The results of experiment ❶ are shown below in figure 4.10. Each of the four plots contains 20 normalized RSMUAPs estimated from stage 9 SEMGs contaminated by a different amount of coloured Gaussian noise. On each plot, the mean variance between estimated RSMUAPs is shown. These plots reflect the effect of decreasing SNR on the bicepstral deconvolution algorithm.

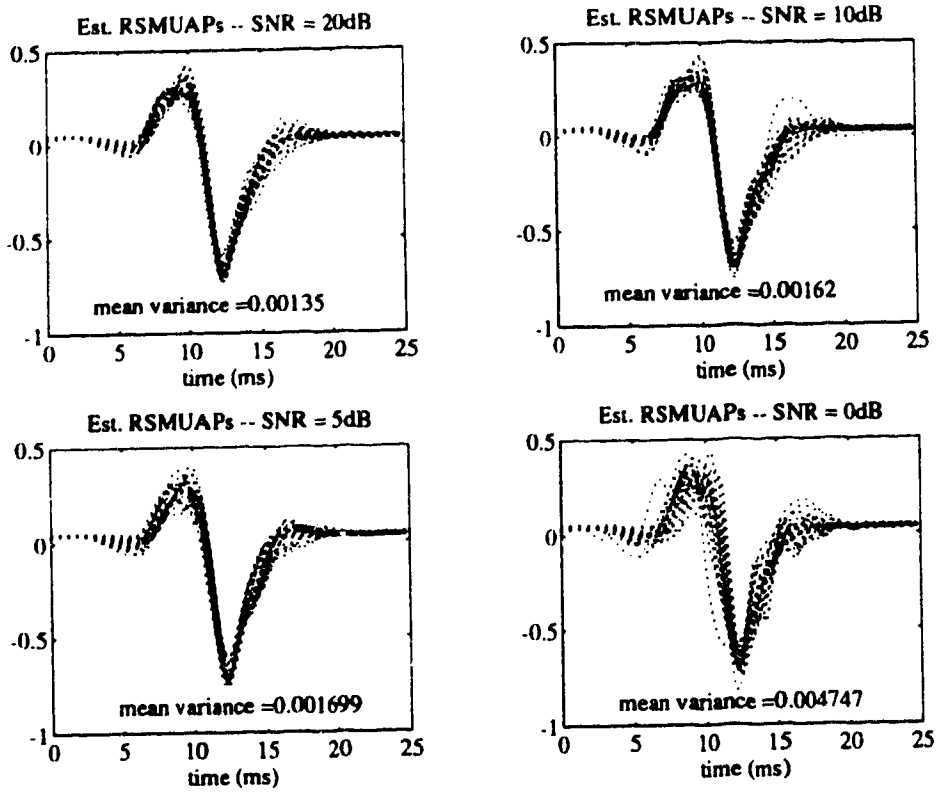


**Figure 4.10** Noisy RSMUAPs. 20 Estimated RSMUAPs per plot, from 20 noisy SEMGs with varying SNRs.

Figures 4.11, 4.12, and 4.13 show the results of experiment ❶. Much like figures 4.4, 4.5, and 4.6, these plots each contain 10 estimated RSMUAPs and one ideal RSMUAP from stage 1, 5 and 9 SEMGs, respectively. However, these RSMUAPs are estimated from model B SEMGs. The appearance of these RSMUAPs, both estimated and ideal, do not differ significantly from the RSMUAPs derived from model A simulations.

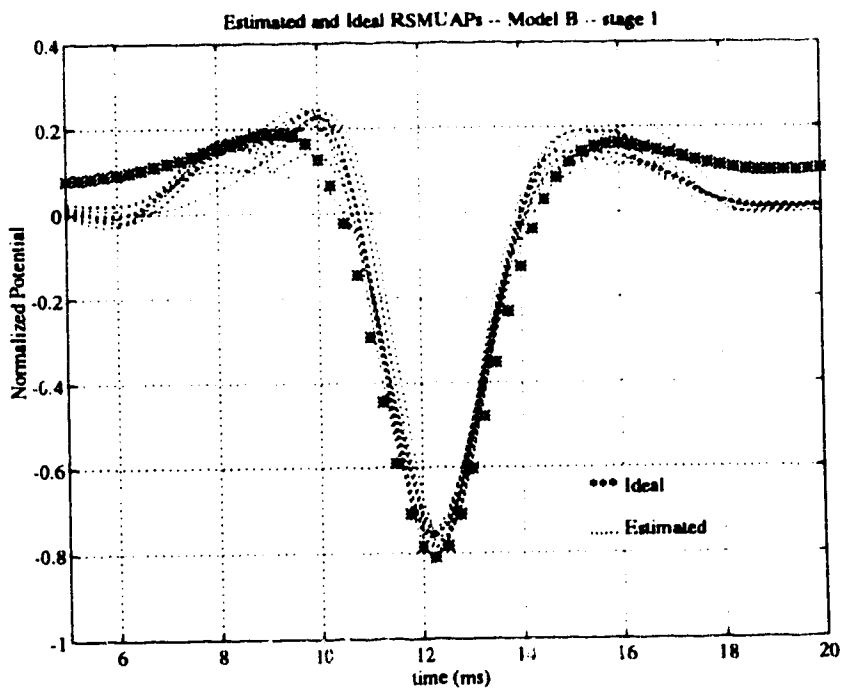


**Figure 4.11** Stage 1 Model B RSMUAPs. Ten estimated RSMUAPs and one ideal RSMUAP from model B stage 1 SEMGs.

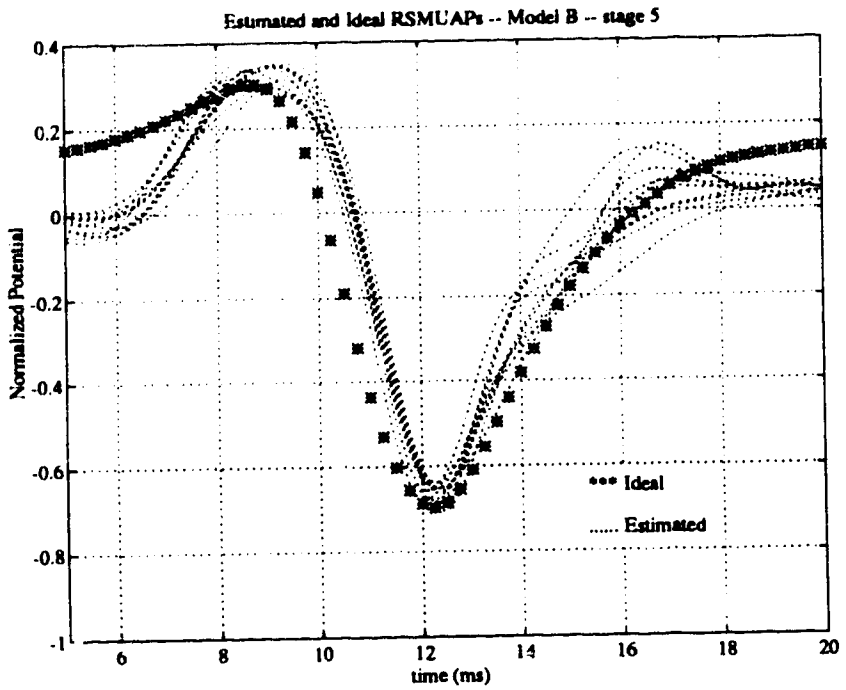


**Figure 4.12** Stage 5 Model B RSMUAPs. Ten estimated RSMUAPs and one ideal RSMUAP from model B stage 5 SEMGs.

The effects of a decreasing firing frequency (experiment ●) on the SEMG and subsequent RSMUAP estimations are shown in figures 4.14 and 4.15. The first figure (4.14) contains the magnitudes of the bispectra of both the stationary and non-stationary simulated firing signals. There is little or no discernable difference between the two bispectra, indicating that the non-stationary firing sequence may not interfere with the bicepstral decovolution process.

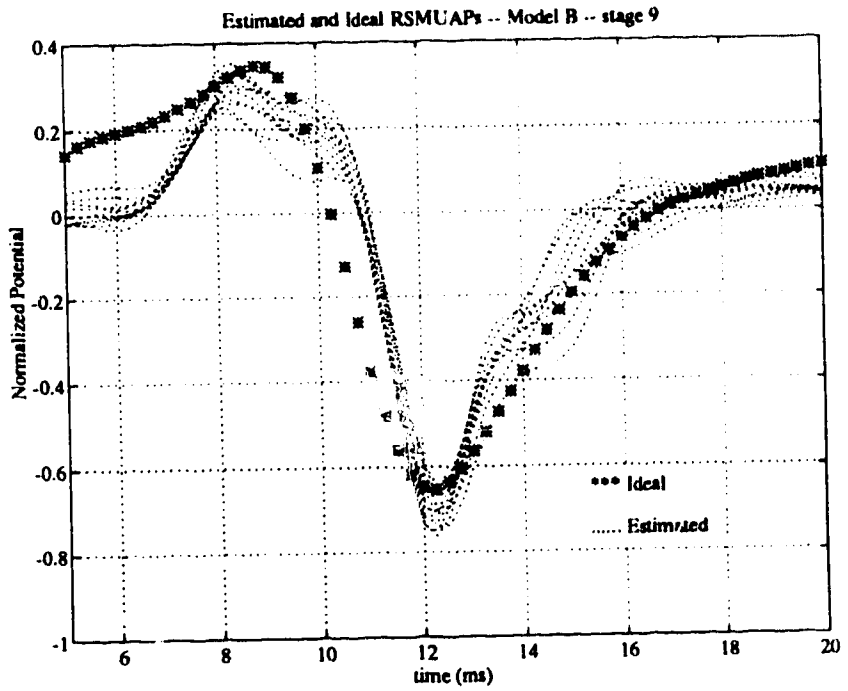


**Figure 4.13** Stage 9 Model B RSMUAPs. Ten estimated RSMUAPs and one ideal RSMUAP from model B stage 9 SEMGs.

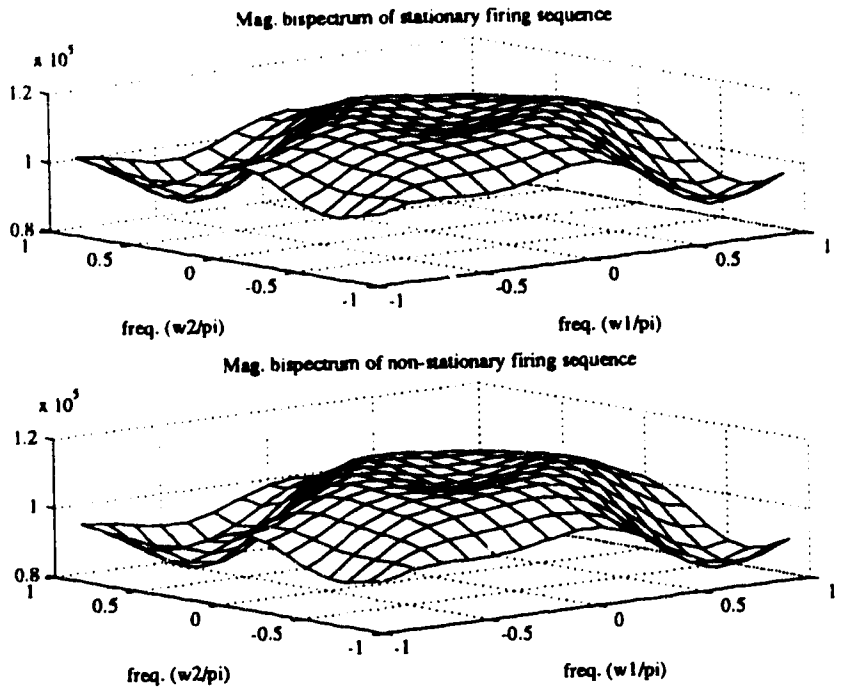


re 4.14 The magnitude bispectra of stationary and non-stationary firing

The six plots in figure 4.15 each show 10 normalized RSMUAPs. The left column contains plots of RSMUAPs estimated from normally simulated SEMGs, while the right column contains RSMUAPs estimated from the same SEMGs after applying a linear gradient to their firing signals. As expected from figure 4.14, the non-stationary firing sequence has caused no noticeable change in the ability to estimate the RSMUAP.

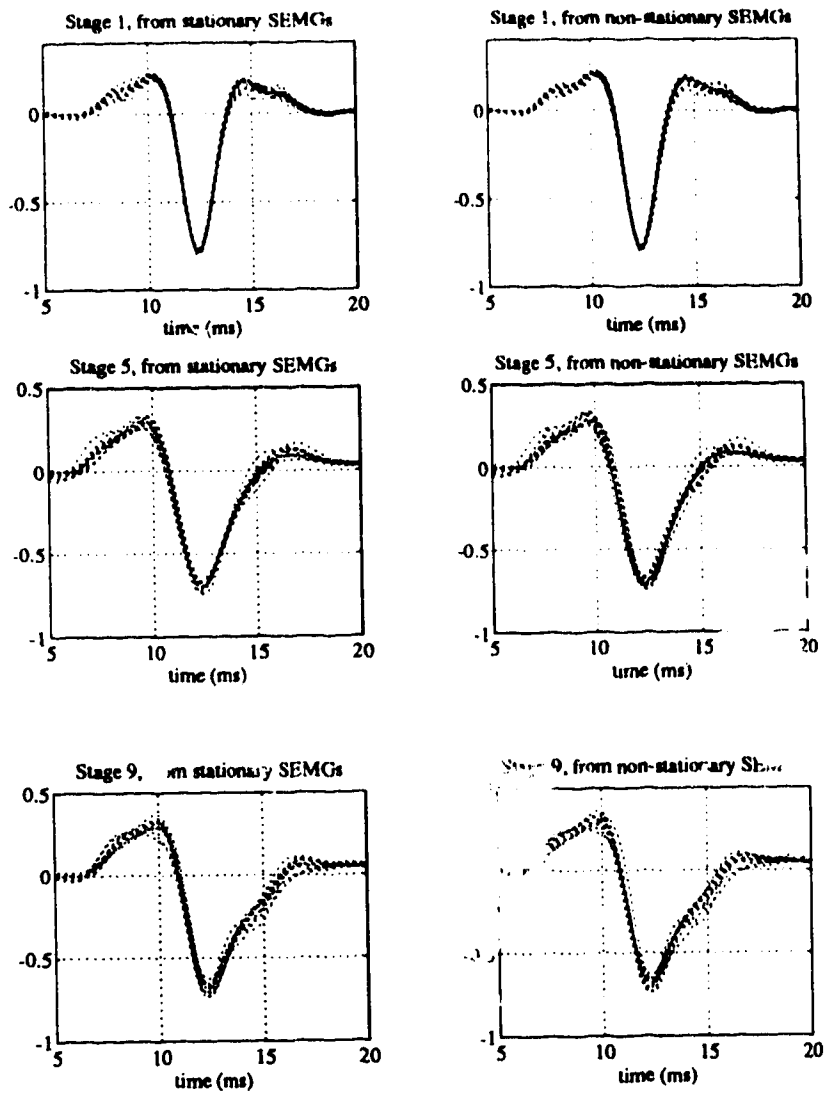


**Figure 4.15** Estimated RSMUAPs from SEMGs with stationary and non-stationary firing signals

# Chapter 5
# Discussion

*Introduction*

The objective of this thesis is to assess the merit of bicepstral deconvolution as a tool for analyzing the SEMG. This assessment hinges on the procedure's ability to estimate RSMUAPs, the quality of these estimates, and, most importantly, the meaning of these estimates. Discussing these criteria is done by examining the following questions. Do estimated RSMUAPs provide a valuable representation of the SMUAPs and of the pathophysiologic state of the muscle? What advantages are found by assessing muscle using estimated RSMUAPs as opposed to needle measured MUAPs, or other SEMG analysis techniques? Is bicepstral deconvolution an effective method of estimating RSMUAPs? And, how are results found in this thesis dependent upon the SEMG modelling developed herein? Finally, ideas for future SEMG research that have become apparent in the creation of this thesis are discussed.

*RSMUAPs' Reflection of Myopathy*

Without thoroughly examining the inverse problem of bioelectric phenomenon, it is difficult to say exactly what information the estimated RSMUAP contains; however, through the experiments in chapter 4, it is clear that it does, quite consistently, reflect myopathic progression. Comparing figures 4.4 through 4.6, distinctly different shapes appear in the ideal RSMUAPs for myopathy stages 1, 5, and 9, and, although not shown, the same is true for all nine stages of myopathic progression. Clearly then, the ideal RSMUAP contains valuable information about the state of a muscle afflicted with a myopathy. From the same figures, it is seen that the estimated RSMUAPs change due to myopathic progression in the same manner as their ideal counter parts. A more quantitative measure of the estimated RSMUAP's ability to reflect myopathic progression lies in the results of the discriminant analysis.

Tables 4.1 and 4.2 indicate that it is possible to classify, with reasonable accuracy, the state of a muscle afflicted with a myopathy given an estimated RSMUAP, and a training set of data. Although table 4.1 shows that RSMUAPs from stages 5 through 9 are classified correctly no better than 50% of the time, one must remember that the division of myopathic progression into 9 stages is purely arbitrary. If an RSMUAP classification is considered correct if the observation is placed plus or minus one group from the group it belongs, then the above discriminant analysis looks much better. Using this loosened constraint of correct classification, the percentage of RSMUAPs correctly classified for observations from each of the nine groups is listed in table 4.2. For example, 86% of the SEMGs from stage 5 are classified as being a stage 4, 5, or 6. Averaging across the entire data set then shows that 86.67% of RSMUAPs are correctly classified.

*RSMUAPs versus MUAPs*

The most obvious motivation for assessing muscle using RSMUAPs instead of MUAPs is that the former are obtained non-invasively. Invasive measures, as discussed in chapter 1, are more than simply unpleasant for the patient, but fundamentally problematic in that they disturb the state of the system that is being measured. In addition, however, there are diagnostic advantages in using the SEMG instead of needle EMG.

In the case of the needle EMG tests that are used to measure MUAPs, there is a huge amount of variability between measures because the exact MUAP shape is highly dependent upon the relative position of the needle to the contributing muscle fibres. For each needle insertion a given MUAP is unique, and possibly quite different. For this reason, several needle insertions are normally required to identify enough MUAPs to make an assessment of the muscle, especially if a quantitative or automated assessment is desired. For example, it is not the existence but rather the increase in polyphasic activity that Konec uses for automatic assessment of needle EMG [5]. That is, a certain percentage of MUAPs are expected to be polyphasic in any muscle due to the inherent variability of the MUAP. As evidenced in the previous section, however, the RSMUAPs reflect changes due to myopathic progression in a consistent and predictable manner.

A possibly more important scrutinization of the RSMUAP comes with respect to other SEMG analysis methods. The goal, recall from chapter 1, of pursuing the RSMUAP was to extract action potential like information from a SEMG. Most other SEMG analysis methods are based on somewhat abstract signal characteristics such as the mean or median frequency. In a recent publication by Priez et. al. [20], 25 characteristics of the power spectrum, including total power, mean and median frequency, and spectral skewness and kurtosis are used in a discriminant analysis to identify and index Duchenne muscular dystrophy. This thesis asserts that, using RSMUAPs, the same identification and indexing could be performed, *and* the data being used would contain intuitive, concrete information: the RSMUAP is more directly representative of the MUAPs than any number of abstract power spectral characteristics.

In the case of the SEMG, there is clearly no way to determine information about a small number of muscle fibres, or to examine the functioning of a single MU. However, a broad evaluation of the muscle is generally desired, for which the SEMG is naturally suited. And now, given the ability to estimate RSMUAPs, the SEMG may be more desirable than the needle EMG in almost all situations.

*Bicepstral Deconvolution for Estimating RSMUAPs*

The first, and most important quality of the bicepstral deconvolution algorithm is that it is based on higher order spectra, which allows for non-minimum phase estimation of a system impulse response. Without this allowance, estimating an RSMUAP would not be possible, and the minimum phase impulse response would be just another abstract statistic of the power spectrum. However, while a higher order technique was required to estimate the RSMUAP, it came with a secondary, and quite significant, benefit. Not only does the bispectrum provide a reliable and flexible method for phase estimation, but it also has the enormous benefit of suppressing Gaussian signals, making it ideal for analyzing non-Gaussian signals corrupted with Gaussian noise.

Two characteristics of the noise are of concern in determining its effect on RSMUAP estimation: the colour and the skew. The skew of the noise dictates the magnitude of the bispectrum. A purely Gaussian noise signal has zero skew, and

therefore, zero bispectrum. The amount of colour in the noise, on the other hand, dictates the flatness of its bispectrum. A white noise signal has a perfectly flat bispectrum, which only presents a scaling factor to the SEMG bispectrum. These two properties mean that noise can deviate significantly from being Gaussian if it is very close to being white, although this quality is not restricted to higher order spectra, as the power spectrum of a white random sequence is flat as well. More importantly, with the bispectrum, the noise signal can deviate significantly from being white, if it is close to being Gaussian.

Assuming that the noise is coloured and additive to the SEMG, the magnitude of its bispectrum is proportional to its skew, as demonstrated by equation (2.59). The contribution of the noise to the bispectrum of the SEMG is then only significant if the magnitude of the skew of the noise is significant with respect to the magnitude of the skew of the noise-free SEMG. If, on the other hand, the noise is not additive to the output but to the firing sequence, then its effects become significant only if its skew is significant with respect to the skew of the firing sequence. Remembering that the RSMUAPs have a zero mean, while the SEMG amplitude is incorporated into the firing sequence, it is fair to say that the vast majority of the magnitude of the SEMG's bispectrum is due to the firing sequence. This means that the preceding statements can be simplified to say that the effect of coloured noise is only significant, regardless of whether it is additive to the output or the firing sequence, if its skew is significant with respect to the skew of the firing sequence. Figure 3.12 from chapter 3 compares the magnitude bispectrum of a firing sequence and a Gaussian sequence. For the sake of comparison, the Gaussian signal is equal to the firing sequence in mean and variance; however, while the firing sequence has a skew of 0.9, the skew of the Gaussian is only 0.005. This results in a factor of nearly 200 difference between the two magnitude bispectra, which leaves plenty of room for increased skew in the noise.

The experiments discussed in the first section of this chapter were repeated with 10dB's of white Gaussian noise added to the SEMGs. Figures 4.7 through 4.9, much like their noise-free counter parts in figures 4.4 through 4.6, show the estimated RSMUAPs from noisy SEMGs to reflect changes due to myopathic progression in a consistent and predictable manner. Repeating the discriminant analysis for RSMUAPs estimated from noisy SEMG again supports the claim the bicepstral deconvolution operates relatively transparently to white Gaussian noise. Although not as many estimates are classified

exactly, as seen in table 4.3, table 4.4 shows that in the noisy case 86.4% of estimated RSMUAPs are correctly classified as compared to 86.7% in the noise-free case.

Further investigation into the effects of noise shows RSMUAPs estimated from SEMGs containing 20, 10, 5, and 0dB of coloured Gaussian noise in figure 4.10. As the SNR drops, the effects of deviation from Gaussianity combined with a large deviation from whiteness become amplified and eventually begin to degrade the RSMUAP estimations. It is not, however, until the SNR is somewhere between 5dB and 0dB that a significant increase in variance occurs. In terms of average power, 5dB and 0dB corresspond to signal to noise ratios of 3.16 and 1.00 respectively, and it is unlikely that such low SNRs would be encountered clinically.

It seems quite reasonable then to conclude that the use of higher order spectra as a conduit for estimating RSMUAPs is not only necessary to provide phase information, but also extremely beneficial in dealing with noise. Several algorithms based on higher order spectra exist that can be used to estimate RSMUAPs, but the bicepstral method is chosen here because it is non-parametric, and does not require estimation of the bispectrum. No further investigation into other methods is made. Also, no real effort is made to optimize the bicepstral algorithm except through empirical means.

*Modelling Variations*

The assessment of bicepstral deconvolution in this thesis is done using simulated data generated on the basis of the synthesis model developed in chapter 3. In order for the results of this study to be of some general value, the influence of this model on the results must be unveiled. The modelling in chapter 3 attempts to represent a SEMG as accurately as possible, while still maintaining enough simplicity to allow straightforward numerical SEMG simulation. Still, assumptions are made regarding the physical structure of muscle that limit the type of muscle the model can represent, and simplifications are made about the motor neuron signals that may effect the deconvolution algorithm.

The development of the SEMG synthesis model is full of rather arbitrary choices for physical characteristics of muscle. For instance, the entire model is based upon the brachial biceps muscle, but it is desirable to know if bicepstral deconvolution is equally as

effective in extracting meaningful RSMUAPs from other muscle's SEMG. Furthermore, the values chosen for mean fiber diameter, and number of fibers per motor unit are disputable quantities. One could do a lengthy study on the effect of every model parameter on the resulting ideal and estimated RSMUAPs, but here the goal is simply to ensure that the ability to estimate RSMUAPs from SEMGs is strictly dependent upon the particular model used herein. This is done by creating a second model, model B, as described in chapter 4, and repeating the RSMUAP estimation experiments.

RSMUAPs estimated from model B generated SEMGs are compared to their ideal counter parts in figures 4.13 through 4.15, as done in figures 4.4 through 4.6 for model A data. For stage 1 very little difference exists between the model A and model B results. In stages 5 and 9, however, there is a noticeable difference in the shape of both the ideal and estimated RSMUAPs between models A and B. For both stages, although more obvious in stage 9, the first phase of the RSMUAP is wider and the last phase is lower for model B. Although it is not of particular concern here why exactly that happens, it is important to note that RSMUAP shapes are dependent, to some degree, on the physical characteristic of the muscle in question. This means that building a data base of RSMUAPs would require reasonably good knowledge, not just of the pathophysiologic state of the muscle, but also the physical structure of the muscle, for each RSMUAP.

Of greater interest with regards to model B SEMGs is whether or not the effect of myopathic progression is reflected in the estimated RSMUAPs. Essentially, the RSMUAPs estimated from model B SEMGs follow a consistent and predictable pattern in all three stages and clearly show change between stages. There is, however, a noticeable increase in variance between estimations for model B. This is likely due to there being fewer muscle fibers being averaged into every SMUAP, which results from model B starting (i.e., stage 1) with roughly 25% fewer fibres per MU and because its smaller diameter fibres become inactive more quickly. If these are the reasons for increased variance, then increased data length should work to reduce that variance, making it a relatively trivial problem. So, while the RSMUAPs generated by model A are not necessarily prototypical, there is no reason to assume that the ability to estimate them is unique.

The other significant simplification made in model A is that SEMGs during a maximal voluntary contraction are stationary over all time. With reference to the linear

system model created in chapter 3 the assumption of SEMG stationarity requires that the system's impulse response be time invariant and its input signal be stationary, where the impulse response is the RSMUAP and the input signal is firing sequence. Without a doubt, the assumption that motor neuron firing patterns are time invariant is not valid [12,19], although most EMG studies indicating this have been done using submaximal contraction. A study by Pinelli et. al., however, tracked MU firing patterns during maximal voluntary contraction over a period of sixty seconds [45]. The results show that maximum discharge frequency of single MUs drop rapidly during the first 2 to 10 seconds from around 50 per second to roughly 25 per second. Following that, the maximum discharge frequency slowly drops to about 15 per second over the next 50 seconds. The question to answer is then, how motor neuron firing pattern variations with time effect bicepstral deconvolution.

Ideally, bicepstral deconvolution should not be affected by the non-stationarity of the motor neuron firing patterns. Regardless of the rate of firing, the input signal, $u(n)$, to the linear system model of the SEMG is still a non-Gaussian random process. Paiss and Inbar determined that the SEMG is stationary of periods of 0.64 seconds [19], which is much longer than the 256 ms long segments from which the third order cumulant sequences are computed. Therefore, over each segment, the SEMG signal is stationary, and the entire contribution of the firing pattern manifests as an impulse of magnitude $A \cdot \beta$ at the origin. Verifying that non-stationary firing sequences do not appreciably effect bicepstral deconvolution is done by modifying the SEMG simulations. In these simulations a gradient is applied to the mean firing frequency of all MUs. The mean interpulse intervals are linearly increased from 60ms to 84ms over a ten second period, which is an increase of three standard deviations from the mean, representing a much steeper gradient than can be inferred from Pinelli's work.

The magnitude bispectra of stationary and non-stationary firing sequences are shown in figure 4.14 to be almost identical. Not surprisingly then, the plots in figure 4.15 show no discernible difference between estimated RSMUAPs from SEMG with stationary and non-stationary firing sequences. Therefore, one may conclude that firing frequency decline due to fatigue has no effect on the ability to estimate RSMUAPs from SEMG.

Of more concern with regards to fatigue and SEMG stationarity is the time-invariance, or lack there of, of the RSMUAPs. If fatigue causes RSMUAPs to change shape over the duration of the SEMG data length, then the resulting RSMUAP estimate will be an average of the RSMUAPs from each 256ms data segment. This may cause problems in the interpretation of RSMUAPs because changes due to fatigue must not be confused with changes due to pathology. Muscle fatigue h . been shown to result in a shift to lower frequencies of the power spectrum, as well as decreased firing frequency [12]. The shift of the power spectrum, which also occurs due to myopathies, is likely due to decreased conduction velocity in the muscle fibers caused by metabolite build up [19]. Avoiding confusion can be done simply be acquiring the total length of SEMG data in several short time segments, allowing the muscle to rest between. However, fatiguing effects on muscle can also be used diagnostically, as muscles affected by different pathologies have been shown to fatigue differently. In any case the effects of fatigue on the RSMUAP requires more investigation, but does not appear to be a serious problem.

*Conclusion*

This thesis introduces and investigates a new approach to SEMG signal processing. In an attempt to extract MUAP like data from the SEMG, the RSMUAP is defined as the action potential that is representative of all the SMUAPs in a given SEMG. It is then shown that RSMUAPs can be consistently estimated from SEMG using bicepstral deconvolution, which is a homomorphic method based on the bispectrum. The bispectrum is required because it preserves phase information, thereby allowing for non-minimum phase reconstructions of RSMUAPs. Experimentation is done entirely through simulation, in which the SEMG is modelled as a sum of SMUAP trains. Each train of SMAUPs results from the convolution of a SMUAP with a train of impulses representing a motor neuron signal. The SMUAP, in turn, is computed as the sum of SFAPs as seen on the surface of the skin.

The results of the experiments indicate that RSMUAPs provide an effective method of detecting change in muscle due to the progression of myopathy. For each of nine stages of myopathic progression, estimated RSMUAPs are shown to be unique enough to be classified correctly, plus or minus one stage, 86.7% of the time, with a

relatively small training set. Furthermore, estimation of RSMUAPs is shown to be relatively unaffected by noise, due primarily to the use of the bispectrum, which suppresses Gaussian signals, in the estimation process. Finally, altering the modelling parameters without causing serious effects to the RSMUAP estimation indicates that the success of this method is not particular to the model used herein, and therefore, indicates that it may be useful for SEMG in general.

From a clinical perspective, very little is discussed in this thesis. Without a doubt, the next step in the investigation of the utility of RSMUAPs is to apply bicepstral deconvolution to clinically acquired data. It is difficult to say what diagnostic possibilities the RSMUAP holds, but for starters, this thesis indicates that it is well suited for following the progression of a myopathy. The inexpensive, painless nature of SEMG makes this procedure ideal for following the progression of disease with frequent examinations. Further down the road, it may also be possible to build up enough data to perform discriminant analysis on RSMUAPs estimated from SEMGs of unknown origin (i.e., the muscle being afflicted with an unknown disorder). It will also be useful to investigate the bioelectric phenomenon involved in RSMUAP formation. That is, if the full potential of the RSMUAP is to be reached, then it must not be treated as an abstract statistic, but rather as an action potential. Understanding the manifestations in the RSMUAP of various pathological changes will help reach that potential.

## REFERENCES


1 R. Rhoades and R. Pflanzer, *Human Physiology*, 1989 Saunders College Publishing

2 F. Buchthal, C. Guld, and P. Rosenfalck, "Action Potential Parameters in Normal Human Muscle and their Dependence on Physical Variables", *Acta Physiologica Scandinavia*, vol. 32, pp. 200-218, 1954

3 A. Fuglsang-Frederiksen, "Quantitative electromyography I. Comparison of different methods", *Electromyography and Clinical Neurophysiology*, vol. 27, pp. 327-333, 1987

4 F. Buchthal, Z. Kamieniecka, and H. Schmalbruch, "Fibre Types in Normal and Diseased Human Muscles and their Physiological Correlates", *Exploratory Concepts in Muscular Dystrophy II*, Editor A. T. Milhorat, Excerpta Medica, Amsterdam, 1974

5 J. Kopec and I. Hausmanowa-Pertusewicz, "Diagnostic Yield of an Automatic Method of Quantitative Electromyography", *Electromyography and Clinical Neurophysiology*, vol. 25, pp. 567-577, 1985

6 C. R. Stewart, S. D. Nandedkar, J. M. Massey, J. M. Gilchrist, P. E. Barkhaus, and D. B. Sanders, "Evaluation of an Automatic Method of Measuring Features of Motor Unit Action Potentials", *Muscle & Nerve*, vol. 12, pp 141-148, 1989

7 L. A. Geddes and L. E. Baker, *Principles of Applied Biomedical Instrumentation, Third Edition*, 1989 Wiley-Interscience

8 D. Stashuk and C. J. Deluca, "Decomposition of surface detected myoelectric signals", *IEEE Eigth Annual Conference of the Engineering in Medicine and Biology Society*, 1986, p. 547

9 M. Hayward, "Analysis of Interference Patterns with Willison's Method -- Clinical uses, Effect of Load, Dynamic Studies", *Electromyography and Clinical Neurophysiology*, vol. 25, pp. 553-556, 1985

10 K. C. McGill, K. L. Cummins, and L. J. Dorfman, "Automatic Decomposition of the Clinical Electromyogram", *IEEE Trans.on Biomedical Engineering*, vol. 32, p 470, 1985

11 H. J. Hermens, K. L. Boon, and G. Zilvold, "The Clinical Use of Surface EMG", *Electromyography and Clinical Neurophysiology*, vol. 24, pp. 243-265, 1984

12 C. J. De Luca, "Physiology and Mathematics of Myoelectric Signals", *IEEE Transactions on Biomedical Engineering*, vol. 26, pp. 313-326, 1979

13 J. Kimura, *Electrodiagnosis in Diseases of Nerve and Muscle: Principles and Practice Ed. 2*, F. A. Davis, Philadelphia, 1989

14 F. Buchthal, F. Erminio, and P. Rosenfalk, "Motor Unit territory in different human muscles", *Acta Physiologica Scandinavia*, vol. 45, pp. 72-87, 1959

15 H. Reucher, G. Rau, J. Silny, "Spatial Filtering of Nonvinvasive Multielectrode EMG Part I -- Introduction to Measuring Technique and Applications", *IEEE Transactions on Biomedical Engineering*, vol. 34, pp. 98-105, 1987

16 K. C. McGill, L. J. Dorfman, J. E. Howard, and E. V. Valainis, "Decomposition of the Surface Electromyogram", *IEEE ninth Conference of the Engineering in Medicine and Biology Society*, pp 2001-2003, 1987

17 A. Blinowska, J. Verroust, and G. Cannet, "The determination of moter units characteristics from the low frequency electromyographic power spectra", *Electromyography and Clinical Neurophysiology*, vol. 19, pp. 281-290, 1979

18 J. L. Coatrieux, "Interference Electromyogram Processing Part I: Influence of the Motor Unit Action Potential Shape on the Interference Electromyogram Spectra", *Electromyography and Clinical Neurophysiology*, vol. 23, pp. 229-242, 1983

19 O. Paiss and G. F. Inbar, "Autoregressive Modeling of Surface EMG and Its Spectrum with Application to Fatique", *IEEE Transactions on Biomedical Engineering*, vol 34, p.761, 1987

20 A. Priez, J. Duchene, and F. Goubel, "Duchenne muscular dystrophy quantification: a multivariate analysis of surface EMG", *Medical & Biological Engineering and Computing*, vol. 30, pp. 283-291, 1992

21 K. Yana, H. Maushima, H. Mino, and N. Takeuchi, "Bispectral Analysis of Filtered Impulse Processes with Applications to the Analysis of Bioelectric Phenomena", *Workshop on Higher-Order Spectral Analysis*, p. 140, 1989

22 G. C. Canovos, *Applied Probability and Statistical Methods*, Little, Brown & Company, 1984

23 C. L. Nikias and M. R. Raghuveer, "Bispectrum Estimation: A Digital Signal Processing Framework", *Proceedings of the IEEE*, vol. 75, no. 7, pp. 869-891, 1987

24 T.S. Rao and M. M. Gabr, *An Introduction to Bispectral Analysis and Bilinear Time Series Models*, Springer-Verlag, 1984

25 A. V. Oppenheim and R. W. Schafer, *Discrete-Time Signal Processing*, Prentice-Hall, 1989

26 R. Pan and C. L. Nikias, "The complex cepstrum of higher order cumulants and nonminimum phase system identification", *IEEE Transactions on Acoustics, Speech, and Signal Processing*, vol. 36, no. 2, pp. 186-205, 1988

27 J. M. Tibolet, *Seismic Applications of Homomorphic Signal Processing*, Prentice-Hall, 1979

28 K. C. McGill and A. Huynh, "A Model of the Surface-Recorded Motor-Unit Action Potential", *IEEE tenth Conference of the Engineering in Medicine and Biology Society*, pp 1697-1699, 1988

29 S. D. Nandedkar and D. B. Sanders, "Simulation of Myopathic Motor Unit Action Potentials", *Muscle & Nerve*, vol. 12, pp 197-202, 1989

30 S. D. Nandedkar, E. V. Stalberg and D. B. Sanders, "Simulation Techniques in Electromyography", *IEEE Transactions on Biomedical Engineering*, vol 32, no. 10, pp. 775-785, 1985

31 Schmalbruch H., *Skeletal Muscle*, Springer-Verlag, Berlin Heildelberg, 1985

32 H. A. Sissons, "Anatomy of the Motor Unit", *Disorders of Voluntary Muscle Ed. 3*, Editor J.N. Walton, Churchill Livingstone, Edinburgh & London, 1974

33 R. Plonsey, *Bioelectric Phenomena*, McGraw-Hill, New York, 1969

34 A. T. Richardson and D. D. Barwick, "Clinical Electromyography", *Disorders of Voluntary Muscle Ed. 3*, Editor J.N. Walton, Churchill Livingstone, Edinburgh & London, 1974

35 Y. Israel and L. Niles, "Muscle Fiber Conduction Velocity and Mean Power Spectrum Frequency in Neuromuscular Disorders and in Fatigue", *Muscle and Nerve*, vol. 15, pp 780-787, 1992

36 V. Dubowitz and M. H. Brooke, *Muscle Biopsy: A Modern Approach*, W.B. Saunders, London, 1973

37 E. Stalberg, "Propagation velocity in human muscle fibre in situ.", *Acta Physiologica Scandanavia*, Vol. 70 (Suppl. 287), pp 1-112, 1966

38 C. J. De Luca C.J, "Physiology and Mathematics of Myoelectric Signals", *IEEE Transactions on Biomedical Engineering*, Vol. 26, No. 6, pp 313-326, 1979

39 J. A. Schmidt and T. C. Pilkington, "The Volume Conductor Effects of Anisotropic Muscle on Body Surface Potentials Using Eccentric Spheres Model", *IEEE Transactions on Biomedical Engineering* vol. 38, no. 3, pp. 300-303. 1991

40 *Mathematical Tables from Handbook of Chemistry and Physics, Tenth Edition*, C. D. Hodgman Editor, Chemical Rubber 1957

41 H. J. Hermens, T. A. M. van Bruggen, C. T. M. Baten, W. L. C. Rutten, and H. B. K. Boom, "The Median Frequency of the Surface EMG Power Spectrum in Relation to Motor Unit Firing and Action Potential Properties", *Journal of Electromyography and Kinesiology*, Vol. 2, No. 1, pp 15-25, 1992

42 D. F. Stegman, T. Gootzen and D. M. Vingerhoets, "The Dominating Role of Finite Muscle and Limb Dimensions in Surface Electromyography", *IEEE eleventh Conference of the Engineering in Medicine and Biology Society*, pp 992-993, 1989

43 P. A. Devijver and J. Kittler, *Pattern Recognition: A Statistical Approach*, Prentice-Hall, 1982

44 P. Pinelli, G. Miscio, and F. Pisano, "Firing Frequency During Maximal Voluntary Contraction", *Electrophysiological Kinesiology, International Congress Series 804*, Elseviers Science Publishers, pp 43-47, 1988